Wave propagation over a submerged bar: benchmarking of VoF, sigma transformation, and SPH numerical models against physical wave flume tests

Andersen, Jacob; Eldrup, Mads Røge; Ferri, Francesco; Verao Fernandez, Gael

Published in:
Discover Applied Sciences

DOI (link to publication from Publisher):
10.1007/s42452-025-06651-9

Publication date:
2025

Document Version
Publisher's PDF, also known as Version of record

Discover Applied Sciences

Research

Wave propagation over a submerged bar: benchmarking of VoF, sigma transformation, and SPH numerical models against physical wave flume tests

Jacob Andersen[1] · Mads Røge Eldrup[1] · Francesco Ferri[1] · Gael Verao Fernandez[1,2]

Received: 2 September 2024 / Accepted: 3 March 2025
Published online: 03 May 2025

Abstract
Accurate prediction of wave transformation is key in the design of coastal and nearshore structures which typically depends on numerical models. Turbulent and rotational effects call for the use of Computational Fluid Dynamics (CFD) solvers of which a large range of formulations including free surface treatments exists. Physical wave flume tests of wave propagation over a submerged bar with various levels of nonlinearity, regularity, and wave-breaking, dedicated to numerical model benchmarking or validation, were carried out in the Ocean and Coastal Engineering Laboratory of Aalborg University. Three fundamentally different CFD models each widespread within their category are benchmarked against the experimental data. The CFD models are based on (i) the Volume of Fluid (VoF) based interFoam solver of OpenFOAM, (ii) the sigma-transformation solver of MIKE 3 Waves Model FM, and (iii) the weakly compressible delta-SPH solver of DualSPHysics. Accuracy of the numerical models is assessed from surface elevation time series, evaluation metrics (averaged errors on surface elevations, amplitudes, phases, and wave set-up), and spectral analyses to calculate the amplitude and phase contents of primary and higher-order components along the wave flume. Applicability is assessed from computational costs and ease-of-use factors such as the effort to configure the numerical models and achieve convergence. In general, the numerical models have high correlation to the physical tests and are as such suitable to model complex wave transformation with an accuracy sufficient for most coastal engineering applications. The VoF model performs more accurately under the turbulent conditions of breaking waves, increasing its relative accuracy in the prediction of downwave surface elevation. The sigma transformation model has simulation times one to two orders of magnitude lower than those of the VoF and SPH models.

Highlights

- Benchmarking of three fundamentally different CFD models, each widely used within their type, against physical validation tests.
- Comparative analysis of the numerical models with emphasis on accuracy and computational costs.
- Datasets from both physical wave flume tests and numerical models are made public for benchmarking/validation by others.

✉ Gael Verao Fernandez, gael.verao-fernandez@tu-braunschweig.de; Jacob Andersen, jacoba@build.aau.dk; Mads Røge Eldrup, mrel@build.aau.dk; Francesco Ferri, ffer@build.aau.dk | [1]Department of the Built Environment, Aalborg University, Thomas Manns Vej 23, Aalborg Ø 9220, Denmark. [2]Present Address: Leichtweiß-Institute for Hydraulic Engineering and Water Resources, Technische Universität Braunschweig, Beethovenstraße 51, Braunschweig 38106, Germany.

Keywords Wave transformation · Shoaling · Breaking · Physical wave flume · CFD

1 Introduction

Accurate prediction of wave transformation is fundamental in the design of coastal infrastructure, including sea dikes, sea walls, breakwaters, and substructures for nearshore wind turbines. The demand for such infrastructure is expected to increase in the coming years owing to climate change and the global energy transition [1, 2]. Wave transformations encompass shoaling, refraction, diffraction, and breaking, and govern design parameters such as wave loads, wave run-up, and sediment transport which are critical for the design of coastal infrastructure. Wave transformations can be highly nonlinear and complex, e.g., from inherently random, turbulent wave-breaking, nonlinear wave-wave interactions, and wave-decomposition (e.g., under deshoaling). Such complex wave transformations cannot be accurately predicted by the otherwise widely used Boussinesq-like equations [3–5] or the shallow water equations [6] forming the basis of many coastal engineering tools for modelling of wave transformation. Multiple correction modules to these models have been developed to account for physical processes not captured with the governing equations—however, with limited accuracy or application range. To reduce the influence from simplifying assumptions in the investigation of complex wave transformation, physical tests or computational fluid dynamics (CFD) models numerically solving the Navier–Stokes equations may be employed. Physical tests in laboratory facilities serve as the most accurate way to represent reality and are vital in the assessment of the accuracy of numerical models. However, physical laboratory tests are expensive and larger test matrices are usually not feasible to investigate through a purely experimental campaign. On the other hand, CFD models allow for a less expensive analysis (e.g., through use of open-source codes) with no inherent uncertainty from measurement equipment. Besides, CFD models have high agility in the test setups, meaning for example the inclusion of different coastal structures can be handled rather easily relative to physical tests. Despite the higher fidelity of CFD models, relative to, e.g., widely applied Boussinesq-like or shallow water equation models, these remain subject to multiple assumptions and rely on accurate physical tests in the validation stages of V&V (verification and validation) procedures preceding any practical application [7]. Verification refers to the assessment of numerical uncertainty from discretization, iterative, and round-off errors, whereas validation refers to the assessment of model errors by comparison to other work - most often physical tests capturing the governing physics of the problem at hand (ASME, 2006).

1.1 High-fidelity numerical modelling of wave transformation

Today, most of the two-phase CFD codes used for engineering purposes employ interface capturing methods with advection of a scalar field that represents the free surface such as the distance to the free surface in Level-Set methods or a volume fraction of water in Volume of Fluid (VoF) methods [8, 9]. Within the topic of complex wave transformation including wave-breaking, the VoF-based, incompressible interFoam solver under the open-source framework OpenFOAM [10] is a highly popular and commonly used to solve the Unsteady Reynolds-Averaged Navier–Stokes (URANS) equations with closure from a turbulence model as in, e.g., [11–15]. Brown et al. [16] investigated the performance of interFoam with several popular turbulence models against physical tests with spilling and plunging breaking waves by Ting and Kirby [17]. Brown et al. highlighted the importance of the choice of turbulence model and recommended the nonlinear $k-\varepsilon$ model by Shih et al. [18]. The interFoam solver has somewhat high requirements for spatial and temporal resolutions for accurate performance in wave propagation applications [19, 20]. Erroneous behaviour of interface wiggles, overestimation of crest velocities, and spurious air velocities have been reported predominantly at moderate to low resolutions [8, 21, 22]. The VoF method assumes a smooth density variation at the interface. However, for air-water interfaces the density gradient is very large and consequently not resolved which has been shown to cause an imbalance of the momentum equation at the air-water interface [23, 24] presumably leading the high requirements to resolution. Due to the high density ratio between water and air, the solution of the air phase is insignificant in the simulation of wave propagation in most coastal applications, i.e., where air entrainment is unimportant [21]. Based on this, single-phase solvers pose a feasible alternative to two-phase solvers in simulation of wave propagation as air velocities is often limiting time steps using maximum Courant-Friedrichs-Lewy (CFL) conditions and the number of cells is decreased. Besides, directly imposing boundary conditions at the free surface can increase accuracy and mitigate the requirements for high resolutions at the interface in VoF methods [24, 25]. A computationally efficient method to achieve this is to transform the vertical coordinate into a sigma coordinate which encompasses the free surface and bathymetry [26]. A single-phase URANS solver utilizing the sigma-transformation approach is the MIKE

3 Wave Model FM [27] from Danish Hydraulic Institute. An important restriction on the sigma-transformation approach is that the free surface must be a single-valued function of class C^2, i.e., continuous and two-times differentiable [28], limiting the approach to model energy dissipation without modeling the actual wave-overturning [25].

Up till now, only CFD methods of Eulerian nature have been introduced. However, the Lagrangian method of Smoothed Particle Hydrodynamics (SPH) has grown increasingly popular in the past decade for especially large surface deformation cases within coastal engineering [9]. The SPH method discretises the fluid domain into a set of fully Lagrangian computational points or so-called particles. Hence, the method is meshless with inherent tracking of the free surface avoiding the challenges of (re-)meshing and special treatment of the free surface typically encountered in Eulerian methods. Single-phase models by weakly compressible SPH of the open-source framework DualSPHysics [29] have been applied in several studies on complex wave transformation, e.g., [30–32]. Spurious oscillations in the pressure and density fields of weakly compressible SPH is commonly mitigated by the addition of diffusive terms in the continuity equation referred to as delta-SPH [33]. To increase confidence of the less established method of SPH in CFD relative to mesh-based methods, five grand challenges [34] have been formulated by the international organisation SPHERIC shedding light on challenges in SPH associated to, among others, convergence, consistency, and stability.[34] Moreover, the method remains computationally expensive wherefore graphics processing unit (GPU) acceleration is made available with DualSPHyshics.

As communicated above, the variety of high-fidelity numerical methods to simulate complex wave transformation is vast. Nevertheless, the advantages regarding the accuracy and applicability of the various methods are only scarcely described and, in particular, quantified in literature. Gruwez et al. [35] compared the VoF-based solver interFoam (OpenFOAM), weakly compressible SPH (DualSPHysics), and a nonlinear shallow water equation solver (SWASH) for wave interactions with sea dikes on shallow foreshores. interFoam had the best overall performance but also the highest computational cost while the overall performance of the SPH model was assessed high as well. Wroniszewski et al.[8] inter-compared four VoF-based Navier–Stokes solvers (including interFoam) for solitary wave propagation and run-up on a plane beach. The study found that issues associated with the smeared interface of the interFoam solver (e.g., erroneous crest velocities as previously described in the present section) were mitigated with increasing resolutions but lacked experimental data. González-Cao et al. [35] investigated regular, breaking waves impacting with a vertical sea wall on a steep foreshore with interFoam and weakly compressible SPH from DualSPHysics. For high resolutions, the models were reported to perform similarly in terms of accuracy whereas at low to moderate resolutions interFoam was more accurate. Park et al. [36] benchmarked two VoF-based Navier–Stokes solvers (interFoam and Ansys Fluent) in interactions of non-breaking and breaking waves with elevated coastal structures. The study stressed the importance of the prediction of wave-breaking to accurately capture forces and pressure distributions on coastal structures and found that the models had similar accuracy relative to the physical tests with the highest deviations under breaking wave conditions. The benchmarking was, however, mostly qualitative and focused on two rather similar CFD models.

A strenuous test case for complex wave transformation that to the best of the authors' knowledge has not been used in the benchmarking of multiple CFD models is that of wave propagation over a submerged bar encompassing the complex wave transformations of wave-shoaling, nonlinear wave-wave interaction, wave-breaking, and wave-decomposition. Such wave transformations were investigated in the seminal, experimental work of Beji and Battjes [4] and upscaled by Dingemans [3]. These experiments have been used widely to benchmark lower-fidelity models than CFD as, for example, Boussinesq-like models in [3] or for validation purposes of CFD models in, e.g., [19, 37, 38] with most studies focusing on qualitative comparisons and/or disregarding wave-breaking.

1.2 Aim and structure of paper

The aim of the present paper is to assess the accuracy and applicability of three fundamentally different CFD models, each prevalent within their own category; the VoF-based interFoam solver of OpenFOAM, the sigma-transformation solver of MIKE 3 Waves Model FM, and the weakly compressible delta-SPH solver of DualSPHysics. The comparison is based on wave propagation over a submerged bar under various wave conditions. The models are configured using typical settings and techniques from their respective categories for similar applications. The models are detailed in Sects. 3.1–3.3 and are given the acronyms of i-VoF, M-sigma, and D-SPH, respectively. The numerical models are benchmarked against physical wave flume tests carried out at Aalborg University and inspired by the tests of Beji and Battjes [4]. The tests were used to generate dedicated datasets for numerical model benchmarking, or validation, allowing for the quantification of all physical parameters and measurement uncertainty—information which is rarely given in experimental papers in engineering literature, and, e.g., lacks in the works of Beji and Battjes [4] and Dingemans [3].

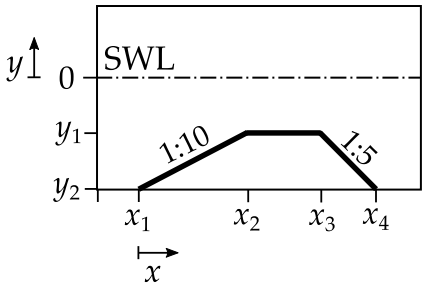

Fig. 1 Submerged bar with coordinates

Table 1 Values of physical parameters of the idealized test case

Parameter	Unit	Value
x_1	mm	0
x_2	mm	1510
x_3	mm	2514
x_4	mm	3261
x_5	mm	147
x_6	mm	300
ρ	kg/m^3	998.2
g	m/s^2	9.82

An idealized test case was formulated to represent the physical tests in an accurate and simple manner aiming to maintain only the aspects of the physical test setup that govern the evolution of the free surface. Numerical models were then set up based on the idealized test case. The reason behind this strategy rather than seeking to do a full 3-D replicate of a physical wave flume was to decrease complexity and, hence, increase practicability to motivate further numerical or even physical tests on the test case by others. Datasets with the results of the physical wave flume tests and all numerical simulations are publicly available from the Zenodo repository of Andersen et al. [39]. To enhance transparency and reproducibility of numerical simulations, the input files of the numerical models are available from this repository as well.

The remainder of the present paper is structured as (i) presentation of the idealized test case, (ii) physical test setup, (iii) governing equations of the numerical models and test setups, (iv) uncertainty analysis of physical tests, (v) definition of evaluation metrics, (vi) convergence analysis of numerical tests, (vii) results with comparisons in both time and frequency domain, snapshots of numerical free surface representation of turbulent bore, and computational costs, (viii) discussion and interpretation of results with regard to the physics of the wave transformations in the test case and benchmarking of the numerical models in terms of both accuracy and applicability, and (ix) conclusions.

1.3 Idealized test case

Consider a fully submerged bar with a trapezoidal cross section. In a two-dimensional Cartesian coordinate system, the bar cross section is uniquely defined from four coordinate sets, see Fig. 1, corresponding to a front slope of 1:10 and a rear slope of 1:5. The bathymetry up- and downwave of the bar is horizontal, and the water depth from the still water level (SWL) to the horizontal bed is $|y_2|$. The water density is ρ and the local acceleration due to gravity is g (Table 1).

Four wave conditions now describe incident, long-crested waves propagating in positive x, see Fig. 1 and Table 2. Wave conditions 1–3 are regular waves with increasing nonlinearity for increasing wave condition number and wave condition 4 is a bichromatic, nonlinear wave. Wave condition 1 can be considered a linear (Airy) wave prior to shoaling, whereas wave condition 2 has significant nonlinearity. Wave conditions 3 and 4 are nonlinear mono- and bichromatic waves, respectively, with plunging wave breaking at the horizontal crest of the bar. The four wave conditions are summarized in Table 2. Boundaries up- and downwave of the bar are assumed far away, therefore the only wave reflection occurring in the idealized test case is from the bar itself.

Table 2 Wave conditions in the idealized test case

Wave condition	Note	H_1 [mm]	H_2 [mm]	T_1 [s]	T_2 [s]
1	Linear	24	–	1.5	–
2	Nonlinear	56	–	1.5	–
3	Breaking	101	–	1.5	–
4	Bichromatic	47	52	1.5	1.0

2 Physical test setup

Physical tests with wave propagation over a submerged bar were carried out in the wave flume of the Ocean and Coastal Engineering Laboratory of Aalborg University, Denmark. A conceptual layout of the physical tests is shown in Fig. 2. The overall dimensions of the wave flume are 22 × 1.5 × 1.5 m. The wave flume has a piston-type wavemaker (mean position at $x_0 = -2813$ mm) with active wave absorption capabilities and passive wave absorption from perforated panels at the end of the flume (starting at $x_5 = 12159$ mm and extending downwave). The coordinates of the bar profile are equal to those presented for the idealized test case in Table 1. Regular waves were generated with approximate stream function wavemaker theory as per Zhang and Schäffer [40] whereas bichromatic waves were generated with second order wavemaker theory as per Schäffer [41] with the adjustments of Eldrup and Lykke Andersen [42].

The submerged bar was constructed out of marine plywood plates supported by three interior wooden rafters which were bolted to the flume floor. Thin metal sheets were installed at the front and rear toe of the bar to avoid flow underneath the bar. Gaps between the bar and flume side walls were sealed with silicone.

Resistance wave gauges were installed at 20 locations in the wave flume, see Fig. 2 and Table 3. Wave gauge numbers (WGnos.) 1–5 and 13–19 were set up in arrays with inter-distances appropriate for reflection analyses. A pressure transmitter (VEGAWELL 52, permanent installation) was used to measure the water depth in the flume. The wave gauges were calibrated with five points over the expected surface elevation measurement range.

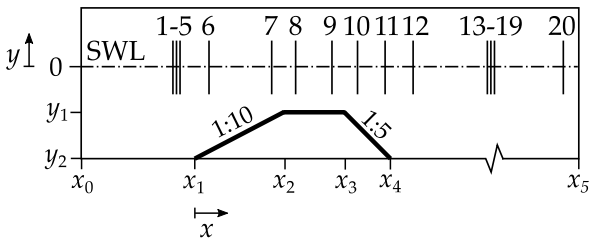

Fig. 2 Conceptual layout of the physical tests. Numbered vertical lines indicate wave gauge locations while bold lines indicate bar geometry. *x* is downscaled by 5 relative to *y* for better overview

Table 3 Coordinates of wave gauges as illustrated in Fig. 2

WGno.	1	2	3	4	5
x [mm]	– 1983	– 1311	– 760	– 453	– 205
WGno.	6	7	8	9	10
x [mm]	199	1300	1708	2305	2707
WGno.	11	12	13	14	15
x [mm]	3051	3460	6703	6775	6890
WGno.	16	17	18	19	20
x [mm]	7172	7461	8023	8690	11966

3 Numerical model fundamentals and test setups

Sects. 3.1–3.3 present the three investigated numerical models which are given the acronyms of i-VoF, M-sigma, and D-SPH, respectively. The numerical models are all based on the Navier–Stokes equations which express the conservation of mass and momentum of a Newtonian fluid. The general Navier–Stokes equations read

$$\begin{aligned} \frac{\partial \rho}{\partial t} + \nabla \cdot \rho U &= 0 \\ \frac{\partial}{\partial t}\rho U + \nabla \cdot (\rho UU) &= \nabla \cdot \tau - \nabla p + \rho g\,, \end{aligned} \tag{1}$$

where U denotes the fluid velocity vector, t the time, ρ the fluid density, p the pressure, g the acceleration due to gravity vector, and τ the viscous stress tensor which under the Stokes hypothesis is given as

$$\tau = \left(\mu\left(\nabla U + (\nabla U)^T\right) - \frac{2}{3}\mu(\nabla \cdot U)I\right) \tag{2}$$

where μ is the dynamic viscosity. Imposing the constraint of incompressibility and constant viscosity, the equations take the form

$$\begin{aligned} \nabla \cdot U &= 0 \\ \frac{\partial U}{\partial t} + \nabla \cdot (UU) &= \nu \nabla^2 U - \frac{1}{\rho}\nabla p + g, \end{aligned} \tag{3}$$

where ν is the kinematic viscosity. The governing equations of the three numerical models are further presented in the following sections. All numerical models are set up as two-dimensional as the geometry is nominally two-dimensional and no scale-resolving methods are employed for turbulence treatment.

3.1 i-VoF (interFoam VoF model)

OpenFOAM [10] is an open-source CFD framework based on the finite volume method (FVM). The i-VoF model is based on the interFoam solver under OpenFOAM v2206 [43] using the incompressible URANS equations with turbulence closure from the nonlinear $k-\varepsilon$ model by Shih et al. [18] as recommended in [16] for breaking waves applications. The incompressible URANS equations are derived from Reynolds-decomposition of Eq. 3 yielding

$$\begin{aligned} \nabla \cdot \bar{U} &= 0 \\ \frac{\partial}{\partial t}\bar{U} + \nabla \cdot \left(\bar{U}\bar{U}\right) &= \nu \nabla^2 \bar{U} - \frac{1}{\rho}\nabla \bar{p} + g - \nabla \cdot \left(\overline{U'U'}\right) \end{aligned} \tag{4}$$

where $\bar{\phi}$ indicates the mean (ensemble average) of the general flow field ϕ and $\phi\prime$ indicates fluctuations. The last term in Eq. 3 is the divergence of the Reynolds stress tensor which by the Boussinesq hypothesis can be accounted for by modelling of a turbulent (eddy) viscosity nu_t that relates the mean strain-rate tensor to the Reynolds stress tensor analogously to how the molecular viscosity relates the mean strain-rate tensor to the mean shear tensor. The nonlinear $k-\varepsilon$ model of [18] utilizes the eddy viscosity assumption but includes a nonlinear stress term τ_{NL} in the Reynolds stress tensor and τ_{NL} goes into the production terms of the transport equations of k and ε [18, 44].

The interFoam solver captures the interface between phases by solving a transport equation for the phase fraction field α which can take on values between 0 and 1, see Eq. 5. Sharpness and boundedness of the interface is handled by a numerical interface compression method, introducing an artificial compression term to the α transport equation (last term in Eq. 5, and the multi-dimensional limiter for explicit solution MULES [21].

$$\frac{\partial \alpha}{\partial t} + \nabla \cdot \alpha U + \nabla \cdot \left(\alpha(1-\alpha)U_r\right) = 0\,, \tag{5}$$

where U_r is a modelled relative velocity vector. Refer to Deshpande et al. [45] for further details on the numerical implementation. Inherent fluid properties are then calculated by the phase fraction as

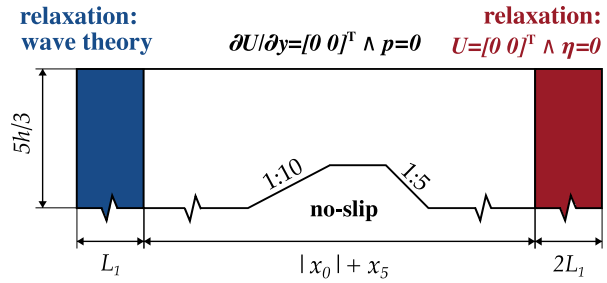

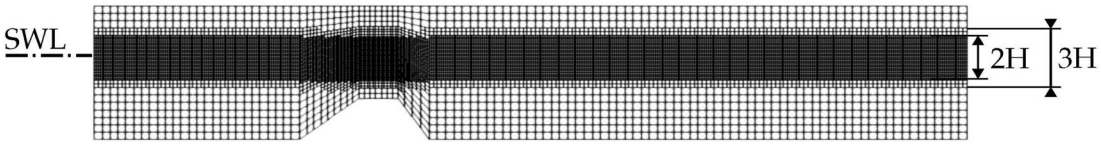

Fig. 3 Domain and BCs for the i-VoF model

Fig. 4 Conceptual layout of mesh with refinement zones (distorted *x*/*y*)

$$\psi = \alpha\psi_1 + (1-\alpha)\psi_2\,, \tag{6}$$

where ψ is any inherent fluid property and subscripts denote different phases.

Wave generation and absorption are handled by the relaxation zone method integrated in the waves2Foam toolbox by Jacobsen et al. [46]. The relaxation zone method weights analytical target solutions ϕ_{target} of the phase fraction and velocity fields with computed solutions ϕ_{comp} at defined zones at the inlet/outlet.

$$\phi = w_R\phi_{comp} + \left(1 - w_R\right)\phi_{target} \tag{7}$$

where $w_R \in [0,1]$ is a relaxation weight distribution taking on values of 0 and 1 at the domain boundary and relaxation zone interface, respectively, and applying the exponential weight distribution as per Fuhrman et al. [47].

Stream function wave theory [48] and second order bichromatic wave theory with wave-wave interaction [49] are employed as target solution in the inlet relaxation zone whereas zero velocity and surface elevation are employed as target solutions for the outlet relaxation zone. The inlet and outlet relaxation zones have lengths of one and two L_1, respectively, see Fig. 3, where L_1 denotes the wavelength from T_1 following linear dispersion. The bar geometry and distances to relaxation zones follows that of the physical test, see Fig. 2 and Table 3, with x_0 and x_5 corresponding to $w_{R=1}$ in the relaxation zones. A no-slip boundary condition (BC) is used for the bed while zero pressure and zero velocity gradient are employed as BCs at the top boundary. Initial conditions (ICs) for velocity, pressure, and phase fraction were chosen to represent stagnant water. The inlet BC and IC for the turbulence kinetic energy k and the turbulence dissipation rate ε were calculated based on Lin and Liu [50] which simulated wave-breaking with the nonlinear $k-\varepsilon$ model of Shih et al. [18]. To allow the production of k (in the k-transport equation) and avoid singularities in the $\varepsilon - transport$ equation small values were seeded at the inlet and initialization. k and ε at the inlet and initialization were calculated from

$$\begin{aligned} k &= \frac{1}{2}\left(I_t L_1/T_1\right)^2 \\ \varepsilon &= C_d\frac{k^2}{\chi\nu} \end{aligned} \tag{8}$$

where L_1/T_1 is the wave celerity and I_t and χ are constants set in accordance with Brown et al. [16]. Brown et al. [16] based the constants on the original work of Lin and Liu [50]. However, at a late stage it was found that the k-equation given in [16] was inconsistent with that of [50], presumably due to a typo; the equation of [16] used I_t instead of I_t^2. As Eq. 8 was primarily applied to seed non-zero values, a simple sensitivity analysis of the values following the equations given in [16] and [50], respectively, were taken on. Only insignificant impacts on the surface elevation time series were detected. Wall functions were adapted for estimation of turbulence fields at the bed and $y^+ \in [30]$ was sustained throughout all simulations.

A structured mesh of predominantly hexahedral-type with two refinement zones around the SWL was used. Cells close to the free surface had aspect ratios of one which is encouraged for simulations of wave breaking with interFoam [46].

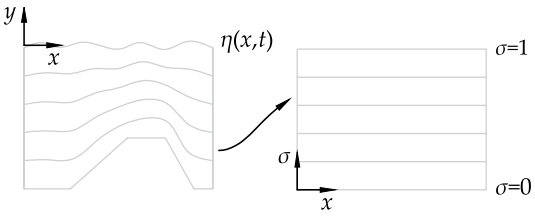

Fig. 5 Concept of the sigma transformation

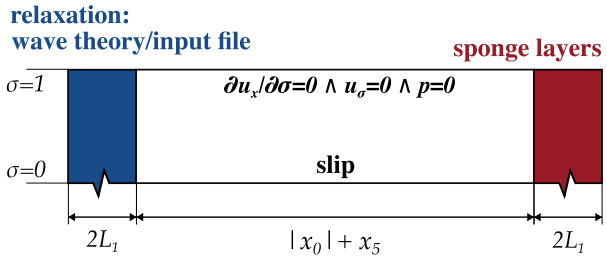

Fig. 6 Domain and BCs for the M-sigma model

The vertical extent of the refinement zones were parameterized with the wave height such that first and second level refinement zones extended ± 2*H* and ±1.5*H* relative to the SWL, respectively, where $H = H_1$ for wave conditions 1–3 and $H = H_1 + H_2$ for wave condition 4, see Fig. 4. Polyhedral cells were used at the refinement zone interfaces.

Variable time stepping was computed from a maximum *CFL* criterion and time marching of the solution was carried out with a first order accurate temporal discretization scheme (backward Euler) to retain stability. Second-order accurate spatial discretization schemes were employed for diffusion, gradient, and Laplacian terms (central-differencing) as well as momentum convection (upwind central-differencing) and phase fraction convection (MUSCL). First-order upwind schemes were applied for the convection of *k* and ε.

3.2 M-sigma (MIKE 3 Waves FM sigma model)

The M-sigma model is based on the MIKE 3 Wave Model FM developed by DHI [27] to solve the incompressible URANS equations, see Eq. 4, with a transformation of the vertical coordinate *y* into the sigma coordinate

$$\sigma = \frac{y + h}{\eta + h}, \tag{9}$$

where *y* has origin at SWL (Fig. 1) and h is the vertical distance from the SWL to the bed. It then follows $\sigma = 0$ at the bed and $\sigma = 1$at the free surface, see Fig. 5.

M-sigma is solved on a structured mesh with equidistantly spaced cells in σ (so-called sigma layers) and *x*, respectively. The convergence with the number of sigma-layers and horizontal faces on the wave transformation are considered in Sect. 6.2.

Wave generation and absorption in the M-sigma model were handled by a relaxation zone upwave of the bar while sponge layers were used for wave absorption downwave of the bar, see Fig. 6. Similarly to the i-VoF model, the domain geometry follows that of the physical test, see Fig. 2 and Table 3, with x_0 corresponding to the end of the relaxation zone and x_5 corresponding to the beginning of the sponge layers.

The implemented relaxation zone technique follows that of the i-VoF model, see Eq. 7, with the same exponential weight function as default. The analytical values were calculated with the built-in stream function wave method of Fenton [48] for the regular waves. For the bichromatic waves no built-in function exists but there is the possibility to provide an input file with amplitudes, frequencies, wavenumbers, phases, and directions for any number of wave components from which surface elevations and kinematics are calculated and superimposed. Wave parameters were calculated by the method of Schäffer [41] and applied as wave generation input for wave condition 4.

The sponge layer technique is based on the method by Larsen & Dancy [51]. In the sponge layer, the surface elevation and the velocities are multiplied with $1/c_s$ where c_s is the sponge coefficient. c_s is close to unity at the beginning of the sponge and increase towards the end following

Table 4 Sponge layer coefficients

N_{sponge} <	κ	ϱ
20	5	0.5
50	7	0.7
100	10	0.85
200	10	0.92
∞	10	0.98

$$c_s = \kappa^{\varrho^i}, \tag{10}$$

where κ and ϱ are constants that depend on the total number of horizontal cells in the sponge layers N_{sponge}, see Table 4, and i is the horizontal cell number with $i = N_{sponge}$ at the start and i=0 at the end. DHI [52] recommends a width of 1–2 wavelengths of the most energetic wave and thus a width of $2L_1$ is applied.

The model uses a variable time step based on a maximum *CFL* criteria. The temporal and spatial discretization schemes were chosen as first order accurate (backwards Euler and upwind, respectively). More details on the numerical solution procedures can be seen in [53]. The interface fluxes are calculated with an approximate Riemann solver. In the M-sigma model, the HLLC solver by Toro et al. [54] is used. The HLLC works as a shock-capture to enhance the stability, which is especially important for simulations with breaking waves.

The $k-\varepsilon$ turbulence model presented by Rodi [55, 56] is employed for closure of the sigma-transformed URANS equations (only $k-\varepsilon$ or $k-\omega$ models are available in MIKE 3 Waves Model FM). The model is extended with buoyancy terms and limiters to stabilize the eddy viscosity in regions where the flow is nearly potential, see Larsen and Fuhrman [57]. Default values are used for the initial conditions of k and ε [52] Initial conditions of η, U, and p were chosen to represent stagnant water.

3.3 D-SPH (DualSPHysics SPH model)

In the SPH method, the fluid is discretized to a set of particles where the field ϕ_i (position, velocity, density, and pressure) of the particle i is calculated as an interpolation of the corresponding field of the neighboring particles j. The contribution of each neighboring particle is determined using a weighting function W_{ij}, referred to as a kernel, with an area of influence depending on a characteristic smoothing length β_h within which fields are interpolated (or smoothed) based on their distance to particle i.

The D-SPH model is based on weakly compressible delta-SPH in the open-source CFD framework DualSPHysics [29]. delta-SPH refers to the inclusion of a numerical density diffusion term (DDT) in the continuity equation to reduce spurious pressure and density fluctuations [33]. The weakly compressible delta-SPH formulation of the compressible Navier–Stokes equations (Eq. 1) can be written in discrete form as

$$\begin{aligned} \frac{d\rho_i}{dt} &= \sum_j m_j \left(U_i - U_j\right) \cdot \nabla_i W_{ij} + D_i \\ \frac{dU_i}{dt} &= -\sum_j m_j \left(\frac{p_j + p_i}{\rho_j \rho_i} + \Pi_{ij}\right) \nabla_i W_{ij} + g, \end{aligned} \tag{11}$$

where t is time, U is the velocity, p is the pressure, ρ is the density, m is the mass, g is the acceleration due to gravity, D is the DDT, and $4\Pi_{ij}$ is an artificial viscosity term. In this study, the Quintic kernel [58] was adopted as W_{ij}. This kernel interpolates fields from neighboring particles within a radius of $2\beta_h$. The DDT proposed by Fourtakas et al. [59] was employed as it has proven to increase the accuracy of the results for the pressure field near the boundaries without compromising the computational time. The artificial viscosity term Π_{ij} proposed by Monaghan [60] was used as a viscous dissipation term depending on the artificial viscosity coefficient γ_v.

Due to the assumption of weak compressibility an equation of state is needed for closure. The Tait's equation with a high speed of sound couples the density and pressure as

$$p = \frac{C^2 \rho_0}{7}\left(\left(\frac{\rho}{\rho_0}\right)^7 - 1\right), \tag{12}$$

where ρ_0 is the reference fluid density, 7 is the polytropic constant and C is the numerical speed of sound at the reference fluid density [61]. This formulation adjusts the fluid compressibility by artificially lowering C resulting in reasonable time steps [61]. Wave generation in D-SPH is generally handled in three different ways: (i) moving boundary particles imitating a physical wavemaker, (ii) relaxation zones, and (iii) open boundaries. For the present study, wave generation method i) with 2nd order wavemaker theory [62] was employed for all regular sea states as it is the standard wave generation method in DualSPHysics (higher order wavemaker theories have not been implemented in current releases). A detailed description of the implementation can be found in [63]. Higher order irregular wavemaker theory is not included in current DualSPHysics releases, and the bichromatic wave of condition 4 was therefore generated from an input file with prescribed motion of the piston-type wavemaker calculated from the irregular second order wave maker theory of Schäffer[41]. The physical wavemaker were adjusted to account for leakage wherefore the logged wavemaker signal were not used as direct input. The free surface is extracted from the D-SPH model where kernels are 40% water based on mass (recommended limit for two-dimensional simulations). In case of multi-valued free surface functions, as seen with plunging waves, the coordinate closest to the bed is extracted (discussed in Sect. 8.2). The two-dimensional domain of the D-SPH model can be seen in Fig. 7. Five layers of boundary particles was used to represent the piston-type wavemaker. The no-slip BC was imposed to the bed which was made up of minimally five layers of boundary particles to ensure proper interaction between the fluid particles and the boundary particles of the bed. At $x = x_5$ a dissipative beach with a slope of 1:16 and horizontal length of $7L_1/2$ was implemented as passive absorption. Additionally, a damping zone was defined with weighting towards stagnant water from a quadratic weighting function along the length of the dissipative beach [63]. Modified Dynamic Boundary Conditions (mDBC) as per English et al. [64] were employed at the wavemaker and bed to mitigate unphysical gaps between boundary and fluid particles otherwise known to occur with the conventional DBC.

4 Uncertainty analysis of physical tests

Measurement uncertainties of the physical tests are accounted for by the construction of uncertainty intervals (UIs) with a 95% level of confidence in Sect. 4.1. Uncertainties of the physical parameters of the idealized test case are given in Sect. 4.2.

4.1 Expanded uncertainty on surface elevation time series

Five repetitions were used for all physical tests. Two-sided 95% UIs around the sample mean surface elevation time series $\bar{\eta}(t)$ were constructed as

$$\bar{\eta}(t) \pm t_{0.95,4} u_{\bar{\eta}}(t) = \bar{\eta}(t) \pm U_{\bar{\eta}}(t), \tag{13}$$

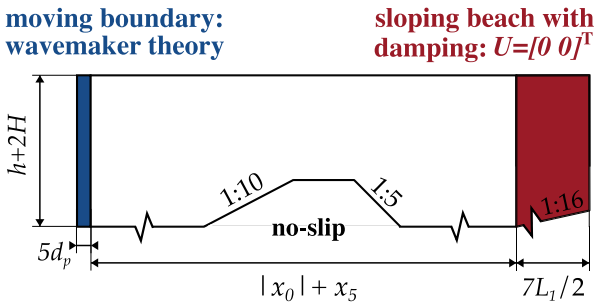

Fig. 7 Domain and BCs for the D-SPH model

where $t_{0.95,4}$ is the Student's t-factor (95% confidence level, 4 degrees of freedom, two-sided), $u_{\bar{\eta}}$ is the combined standard uncertainty, and $U_{\bar{\eta}}$ is the expanded standard uncertainty. The surface elevation η was measured by resistance wave gauges from the linear function

$$\eta = z_2\left(V - V_0\right), \tag{14}$$

where V is the voltage output during testing, V_0 is reference voltage output at SWL (prior to testing), and z_2 is a calibration constant. The uncertainties of the input quantities of Eq. (14) were propagated to η by the law of combination of uncertainty (first order Taylor series approximation) in accordance with [68], which takes the form

$$\begin{aligned} u_\eta^2 &= \left(V - V_0\right)^2 u_{z_2}^2 \\ &+ \left(z_2 - z_2 V_0\right)^2 u_V^2 + \left(z_2 V - z_2\right)^2 u_{V_o}^2. \end{aligned} \tag{15}$$

The discretization uncertainty of the measured voltage is found as a Type B estimate based on the resolution of the signal ($\pm 10V$, 16 bits) and assuming a rectangular distribution within the resolution limits [65]. As V and V_0 are estimated from the sample mean of $N = 5$ repetitions their uncertainties from repeatability were simply taken as the standard deviation of the estimates, i.e.,

$$s_{\bar{X}} = s_X/\sqrt{N}, \tag{16}$$

where $s_{X,N}$ is the sample standard deviation of X. The calibration parameter z_2 and associated uncertainty were estimated using a weighted total least squares (WTLS) approach [66], accounting for uncertainties in the input data (errors-in-variables), on the linear calibration function

$$h^* = z_1 + z_2 V, \tag{17}$$

where h^* denote the water level from a given reference point, z_1 is the intercept, z_2 is the slope, and V is the voltage signal from the wave gauges. The standard uncertainty of the measured h^* was estimated as the maximum of the standard uncertainty of the pressure transmitter (technical datasheet, ISO Type A) and that of a vertically mounted laser distance measurer (declared accuracy of 2 mm, interpreted as the semi-interval, ISO Type B) which was used as a secondary measurement method. The two measurement methods had no detectable deviations in measured water level variations and the maximum standard uncertainty was thus conservatively applied for h^*. The uncertainty of V was taken as the discretization uncertainty. The standard uncertainties of each the input quantity X as given in Eq. 14 and propagated to u_η in Eq. 15 were calculated as the root-sum-square of the elemental uncertainties of X. These are summarized in Table 5.

4.2 Uncertainty of test case parameters

The uncertainty of the physical test parameters which are the basis of the idealized test case are presented in Table 6. These uncertainties have not been propagated into uncertainties on the surface elevation time series (which is non-trivial) and are therefore not included in the constructed 95% UI. Nevertheless, they are given to present the variability of the physical test parameters, i.e., the benchmark. The distances of wave gauges to the mean-position of the piston wavemaker were measured meticulously with a laser distance measurer (declared accuracy of 2 mm). Upper and lower bounds of the measurement process were estimated as ±10 mm. A rectangular distribution with a semi-interval of 10 mm (ISO Type B) around the measured values was assumed to estimate the standard uncertainty of the wave gauge locations—denoted

Table 5 Uncertainty table

X	Note	u_{X_i}	ISO types
V	Resolution	0.15 mV	B
	Repeatability	Eq. 16	A
V_0	Resolution	0.15 mV	B
	Repeatability	Eq. 16	B
z_2	Bias	WTLS	A

Table 6 Uncertainties of parameters from the physical tests

Parameter	Unit	Value	Standard Uncertainty
x_1	mm	0	2.3
x_2	mm	1510	2.3
x_3	mm	2514	2.3
x_4	mm	3261	2.3
x_{WG}	mm	Table 3	5.8
y_1	mm	147	2.3
y_2	mm	300	1.5
ρ	kg/m^3	998.2	0.4
g	m/s^2	9.82	0.003
$H_{1,1}$	mm	24	0.1
$H_{1,2}$	mm	56	0.3
$H_{1,3}$	mm	101	1.2
$H_{1,4}$	mm	47	0.7
$H_{2,4}$	mm	52	1.7

x_{WG} in Table 6. The standard uncertainty of ρ and g are adopted from [67] in which the same laboratory under similar conditions (temperature) were used. y-coordinates were measured at 6 spanwise coordinates between the flume side walls at the toe and the back edge while 5 × 6 measurements were carried out at the bar crest. The standard uncertainties of the y-coordinates were estimated from combining, by root-mean-square, the uncertainty of a laser distance measurer (2 mm semi-interval), used for profiling of the bar, with the standard deviation of y-coordinates from the multiple measurements point at the bar toe and back edge and the horizontal bar crest. x-coordinate measurements were carried out at a single spanwise coordinate and the uncertainties are assumed equal to those of y_2. The uncertainties of H were derived from those of the free surface elevation time series and are given in Table 6 where the first subscript denotes primary/secondary component, and second subscript denotes wave condition. The uncertainties of T are assumed negligible.

5 Evaluation metrics

Surface elevation time series are compared to reference time series quantitively by evaluation metrics. These metrics are utilized in both the convergence analyses of the individual models and in the physical- and inter-model comparison with the only difference being the reference. The evaluation metrics are statistical scalars extracted from a given surface elevation time series $\eta(t)$ and a reference surface elevation time series $\eta_{ref}(t)$. The evaluation metrics include the normalized mean absolute error δ_{direct}, the residual relative standard deviation δ_{std}, the residual correlation coefficient δ_{corr}, and the normalized error on means δ_{mean}. The evaluation metrics are thus selected to represent various error types between signals and are defined in Eqs. 18–21. All evaluation metrics tend to zero when $\eta(t)$ tends to $\eta_{ref}(t)$.

The normalized mean absolute error δ_{direct} reflects the direct absolute difference between two signals, and is given as

$$\delta_{direct} = \frac{\sum_{j=1}^{N} \left|\eta_j - \eta_{ref,j}\right|}{N(\max(\eta) - \min(\eta))}, \tag{18}$$

where N is the total number of data points contained within the analyzed time window. The residual relative standard deviation δ_{std} reflects differences in the amplitude/energy content between two signals with positive values indicating higher energy content in the considered time series than in the reference and vice versa.

$$\delta_{std} = 1 - \frac{\sqrt{\sum_{j=1}^{N} \left(\eta_{ref,j} - \bar{\eta}_{ref}\right)^2}}{\sqrt{\sum_{j=1}^{N} \left(\eta_j - \bar{\eta}\right)^2}}, \tag{19}$$

where the overbar indicates time averaging (rather than ensemble averaging as in Eq. 4). The residual correlation coefficient δ_{corr} reflects phase differences between two signals with values of 1 and 2 signifying zero correlation and anticorrelation, respectively.

$$\delta_{std} = 1 - \frac{\sum_{j=1}^{N} \left(\eta_j - \bar{\eta}\right)\left(\eta_{ref,j} - \bar{\eta}_{ref}\right)}{\sqrt{\sum_{j=1}^{N} \left(\eta_j - \bar{\eta}\right)^2}\sqrt{\sum_{j=1}^{N} \left(\eta_{ref,j} - \bar{\eta}_{ref}\right)^2}}. \tag{20}$$

The normalized error on means δ_{mean} reflects differences in mean water levels from, e.g., wave set-up with positive values indicating a higher mean water level in the considered surface elevation time series relative to the reference.

$$\delta_{mean} = \frac{\bar{\eta} - \bar{\eta}_{ref}}{\max\left(\eta\right) - \min\left(\eta\right)}. \tag{21}$$

6 Convergence of numerical models

The convergence of the three investigated numerical models is accounted for in the present section. The convergence analyses are based on qualitative assessments from surface elevation time series and quantitative assessments from evaluation metrics, see Sect. 5. Surface elevation time series are extracted from wave gauges 5, 7, 10, and 12, representing wave gauge positions upwave of the bar (pre-shoaling), at the bar (shoaling and deshoaling), and downwave of the bar (re-adjustment to horizontal bed), see Fig. 2. Time windows of $2T_1$ are extracted from the second zero-up-crossing after propagation (linear celerity) to the wave gauge position and wave-ramp-up. Only the convergence analyses for wave condition 4 (bichromatic breaking waves) are included in the present section. The convergence analyses of wave conditions 1–3 are included in Appendix A.

6.1 Convergence of i-VoF

A typical normalized measure of the spatial resolution of cell-based numerical models with wave propagation is the number of cells per wave height N_{cH}, e.g., [21, 22], which in the present is adopted as

$$N_{cH} = H/r_c\,, \tag{22}$$

where r_c is the cell size in the finest refinement zone and $H = H_1$ for wave conditions 1–3 and $H = H_1 + H_2$ for wave condition 4. It should be noted that the cell aspect ratio is approximately one and that N_{cH} thus indicate both the horizontal and

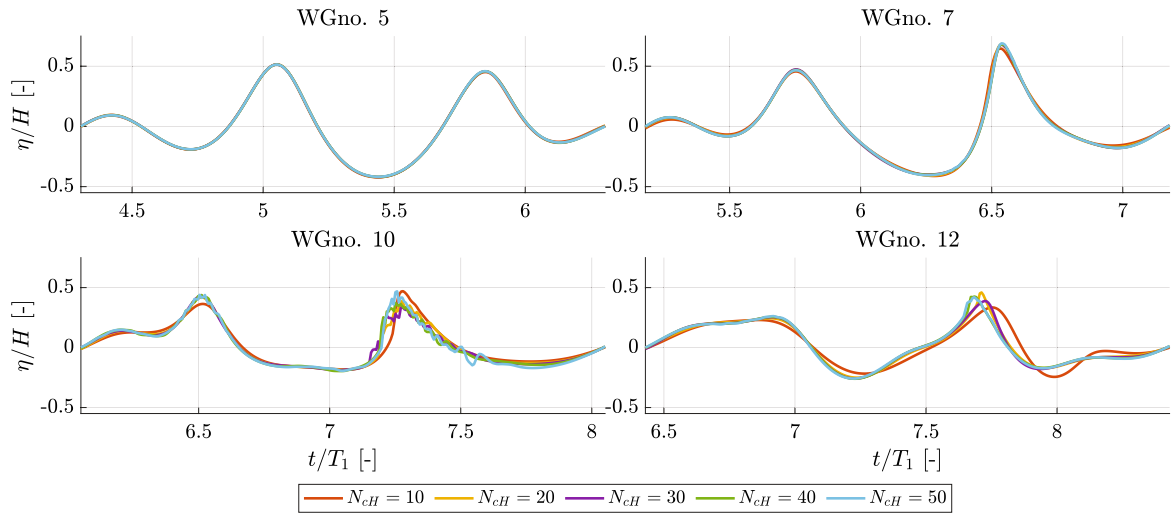

Fig. 8 Influence of N_{cH} on the surface elevation time series for selected WGnos.; wave condition 4 and maximum $C_{FL} = 0.10$

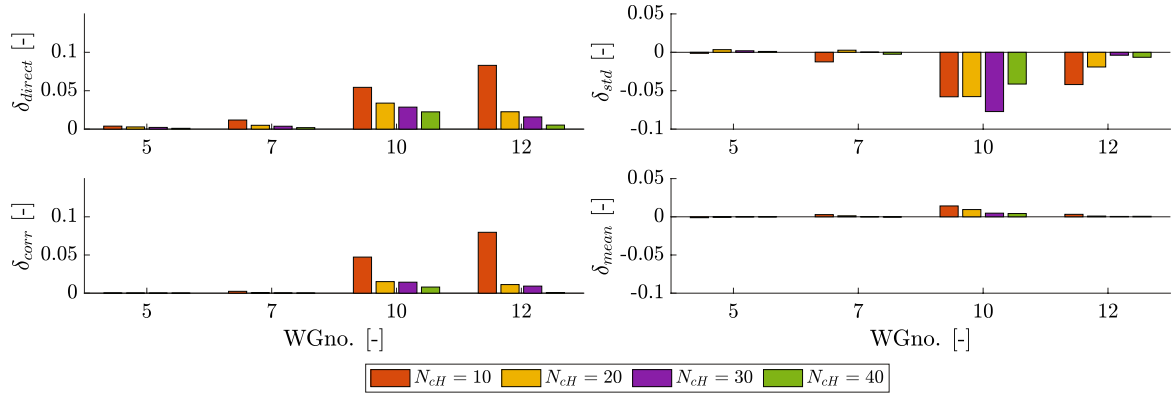

Fig. 9 Influence of N_{cH} on evaluation metrics for selected WGnos.; wave condition 4 and maximum $C_{FL} = 0.10$

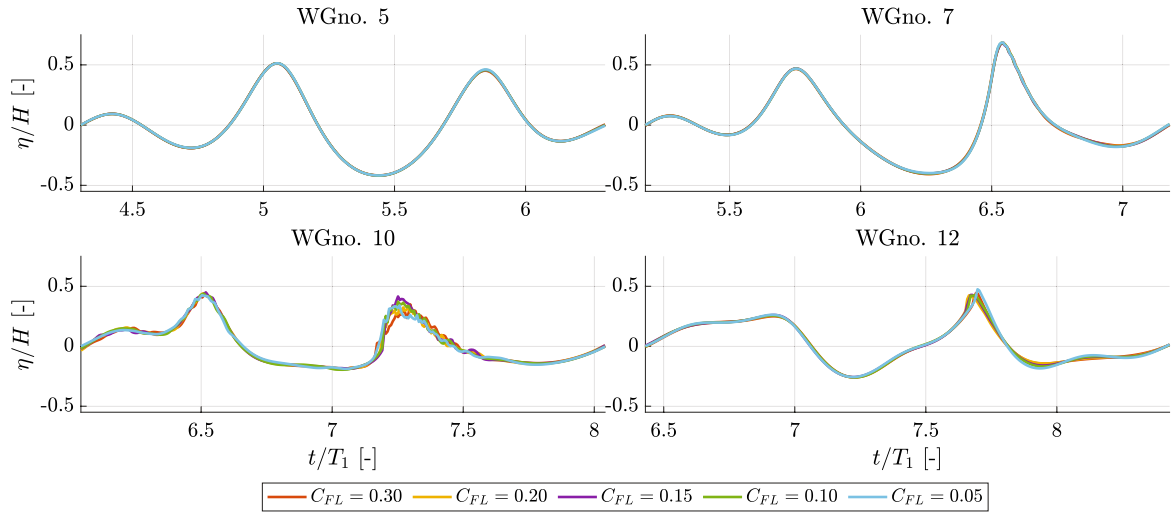

Fig. 10 Influence of maximum C_{FL} on surface elevation time series for selected WGnos.; wave condition 4 and $N_{cH} = 40$

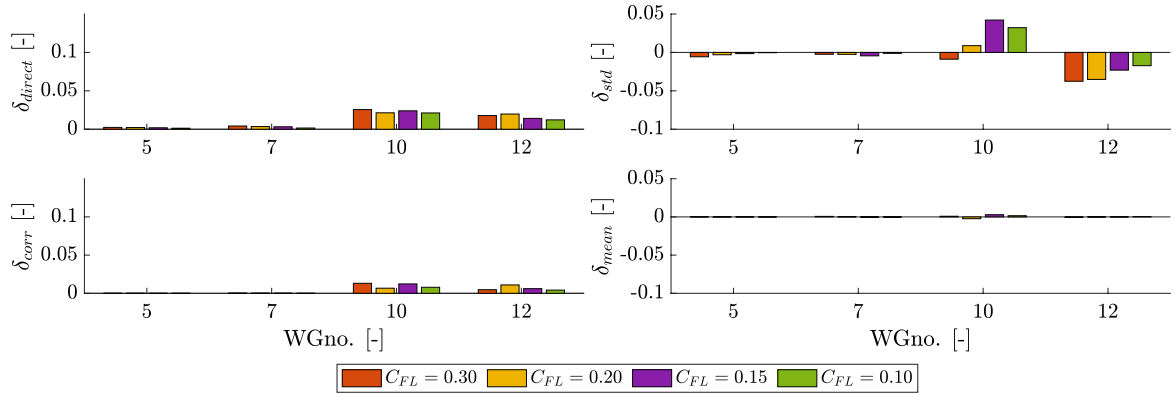

Fig. 11 Influence of maximum C_{FL} on evaluation metrics for selected WGnos.; wave condition 4 and $N_{cH} = 40$

vertical resolutions. As mentioned in Sect. 3.1, maximum C_{FL} criteria were employed for time stepping, wherefore the maximum C_{FL} is used as a measure for the temporal resolution. The spatial resolution was varied with $N_{cH} \in \{10,\ 20,\ 30,\ 40,\ 50\}$ with a constant maximum $C_{FL} = 0.10$ found to be sufficiently small to not lead the discretization error at up to $N_{cH} = 40$. Likewise, the temporal resolution was varied (independently) with a maximum $C_{FL} \in \{0.30,\ 0.20,\ 0.15,\ 0.10,\ 0.05\}$ with

Table 7 Selected N_{cH} and max(C_{FL}) after convergence analysis of each wave condition

Wave condition	N_{cH}	max(C_{FL})
1	10	0.50
2	20	0.40
3	30	0.10
4	40	0.10

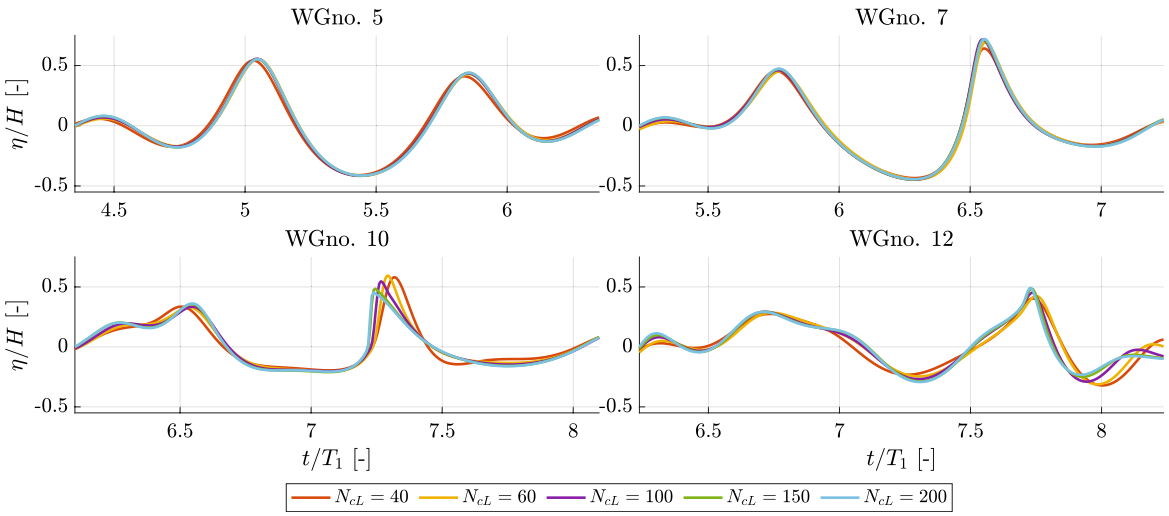

Fig. 12 Influence of N_{cL} on the surface elevation time series for selected WGnos.; wave condition 4 and $N_\sigma = 15$

a constant $N_{cH} = 40$. The finest resolutions were used as references in the calculation of evaluation metrics. The influence of N_{cH} and C_{FL} on the selected surface elevation time series and evaluation metrics are shown in Figs. 8, 9, 10, 11.

While wave propagation seems largely independent of N_{cH} in the tested range at WGnos. 5 and 7 (pre-shoaling and shoaling), the wave breaking is affected significantly by N_{cH} as can be seen from WGno. 10, at $t/T_1 \approx 7.2$. With evaluation metrics well below 5% and surface elevation time series basically indistinguishable, see Figs. 8 and 9, $N_{cH} \geq 40$ is assessed converged. The different numerical diffusive balances obtained with meshes of lower N_{cH} spur delayed breaking onsets and differences from the decomposed waves downwave of the bar at WGno. 12 can be detected, see WGnos. 10 and 12 in Fig. 8. The variation of maximum C_{FL} affects the surface elevation time series and evaluation metrics less than N_{cH} over the tested ranges. The breaking point in the WGno. 10 time series is not altered significantly from C_{FL}, but rather the level of interface wiggles and (partly as a consequence) the amplitude immediately prior to breaking vary with the maximum C_{FL}. These effects are presumably due to the light air phase dictating the time steps with the maximum C_{FL} criterion from which C_{FL} in the water phase remains well below the maximum C_{FL} and the water phase thus remains largely unaltered from the variation hereof. Nonetheless, the erroneous formation of interface wiggles is mitigated by lowering the maximum C_{FL}. The crest height at $t/T_1 \approx 7.2$ at WGno. 10 is approximately 25% smaller with $C_{FL} = 0.30$ relative to $C_{FL} = 0.05$ though $\delta_{std} < 5\%$. Lowering C_{FL} to 0.20 and 0.15 gives a slightly oscillatory convergent behavior in predicting crests at WGnos. 10 and 12 and does not mitigate interface wiggles at the wave crest. $C_{FL} = 0.10$ is assessed sufficiently converged with all evaluation metrics well below 5% and only minor qualitative differences at WGnos. 10 and 12 in Fig. 10. $C_{FL} \geq 0.40$ was also tested and yielded unstable simulations.

Similar analyses were carried out for the i-VoF model with wave conditions 1–3, see Figs. 37, 38, 39, 40, 41, 42, 43, 44 in Appendix A.1. Conclusions are summed up in Table 7.

6.2 Convergence of M-sigma

The horizontal resolution of the M-sigma model is given from the number of cells per wavelength:

$$N_{cL} = L_m / r_{cL}\,, \tag{23}$$

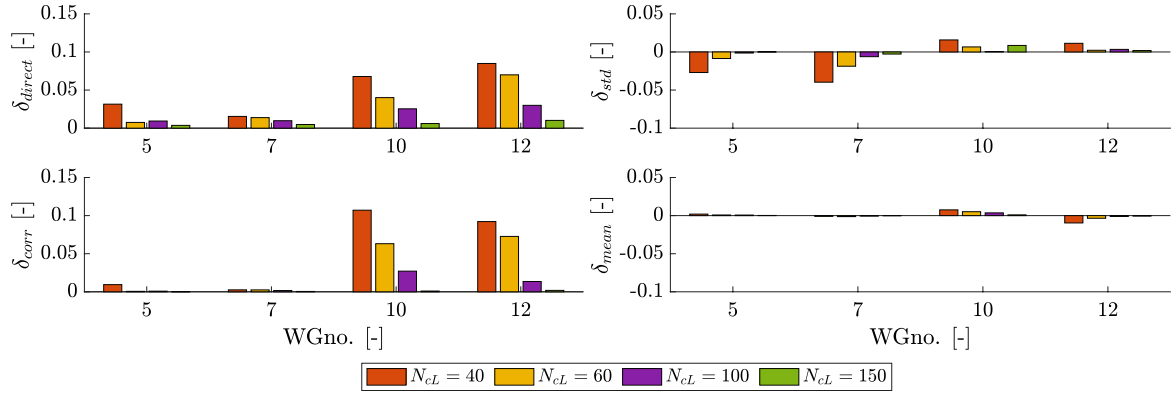

Fig. 13 Influence of N_{cL} on evaluation metrics for selected WGnos.; wave condition 4 and $N_\sigma = 15$

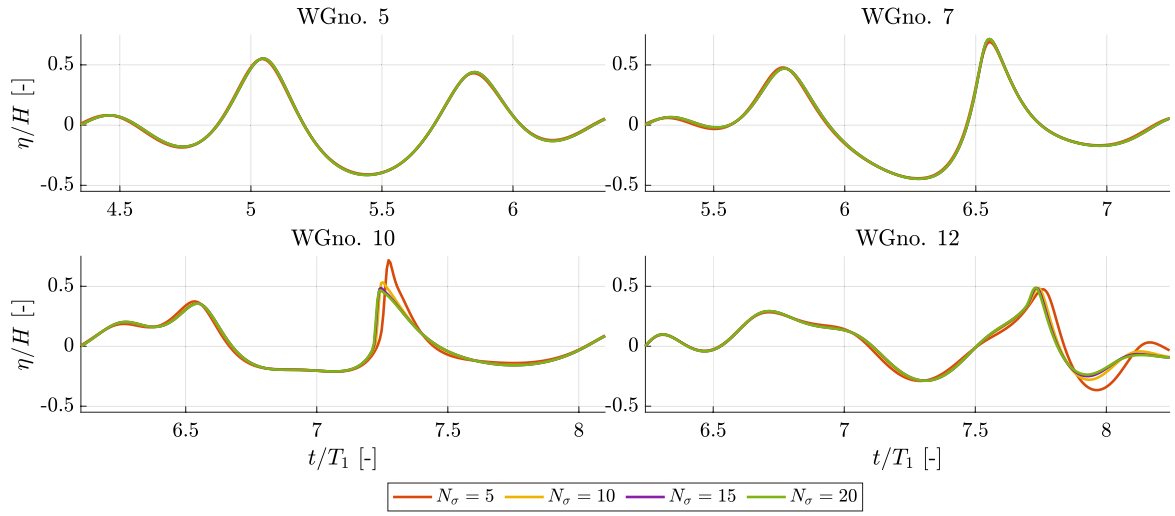

Fig. 14 Influence of N_σ on the surface elevation time series for selected WGnos.; wave condition 4 and $N_{cL} = 150$

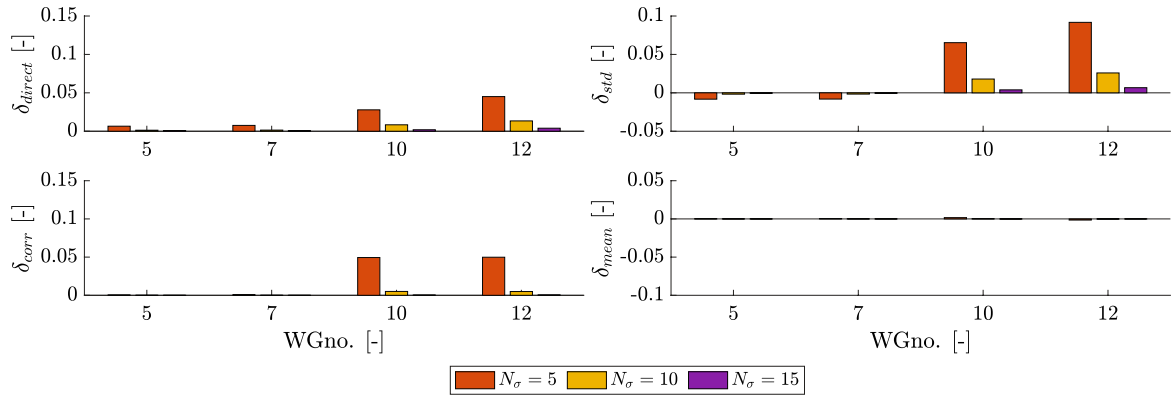

Fig. 15 Influence of N_σ on evaluation metrics for selected WGnos.; wave condition 4 and $N_{cL} = 150$

where N_{cL} is the number of cells horizontally per wavelength, r_{cL} is the horizontal cell size, and L_m is the smallest wavelength in the domain estimated as the wavelength at the horizontal bar crest from T_1 by linear dispersion. The horizontal resolution was varied with $N_{cL} \in \{40,\ 60,\ 80,\ 100,\ 150,\ 200\}$. The vertical resolution is given from N_σ which denotes the number of sigma-layers. The recommended values given by DHI [54] are $N_\sigma = 4 - 7$ for non-breaking waves and $N_\sigma = 8 - 12$ for breaking waves. In the present work $N_\sigma \in \{5,\ 10,\ 15,\ 20\}$ which covers the recommended values. The

Table 8 Selected N_{cL}, N_{σ}, and max(C_{FL}) after convergence analysis of each wave condition

Wave condition	N_{cL}	N_{σ}	max(C_{FL})
1	60	5	0.8
2	100	5	0.8
3	150	15	0.8
4	150	15	0.8

Table 9 Selected N_{pH} after convergence analysis of each wave condition

Wave condition	N_{pH}
1	20
2	20
3	40
4	20

maximum C_{FL} was varied with $C_{FL} \in \{0.8,\ 0.6,\ 0.4\}$ which yielded only negligible variations of surface elevations and associated evaluation metrics, $< 1\%$. A higher maximum C_{FL} criteria was not imposed due to stability reasons. DHI [54] recommends a default value of 0.8. Hence, results with C_{FL} of 0.8 is only shown in the present paper.

The influence of N_{cL} and N_{σ} on the selected surface elevation time series and evaluation metrics are shown in Figs. 12, 13, 14, 15. Figures 12 and 13 show the sensitivity of N_{cL} with $N_{\sigma} = 15$. At WGno. 5, the wave profiles are very similar for all N_{cL} with minor deviations $\delta_{direct} \leq 3\%$. At WGno. 12, this error increases to $> 7\%$ for $N_{cL} \leq 60$. The error is mainly governed by the phase error shown by δ_{corr} which is between $6 - 11\%$. Increasing the horizontal resolution to $N_{cL} = 100$ yields $< 5\%$ for all evaluation metrics. However, from the qualitative assessment of the surface elevation time series in Fig. 12, the shape of the breaking wave at around $t/T_1 = 7.25$ at WGno. 10 differs notably between $N_{cL} = 100$ and $N_{cL} \geq 150$ with an overestimation of the crest elevation of about 20%. Consequently, $N_{cL} = 150$ is assessed converged. Figures 14 and 15 show the sensitivity to N_{σ} using $N_{cL} = 150$. Again, evaluation metrics are largest at WGnos. 10 and 12, but with the variation of the vertical resolution rather than the horizontal, the leading error now shifts from δ_{corr} to δ_{std}. To obtain metrics well below 5%, $N_{\sigma} \geq 10$. However, similar to the variation of N_{cL}, the wave profile and crest elevation at around $t/T_1 = 7.25$ at WGno. 10 varies considerably when comparing $N_{\sigma} = 10$ and $N_{\sigma} \geq 15$ (wave elevation deviation of 13%). Ultimately, M-sigma is assessed converged in wave condition 4 with $N_{cL} = 150$, $N_{\sigma} = 15$, and $C_{FL} = 0.8$.

Similar analyses were carried out for the M-sigma model with wave conditions 1–3, see Figs. 45, 46, 47, 48, 49, 50, 51, 52 in Appendix A.2. Conclusions on the discretization used are summed up in Table 8.

6.3 Convergence of D-SPH

In SPH models, the spatial resolution is given from the initial particle spacing d_p. A typical normalization of the spatial resolution of a meshless-based numerical model with wave propagation is the number of particles per wave height N_{pH}, e.g., [68–70], which in the present is adopted as

$$N_{pH} = H/d_p\ . \tag{24}$$

Using weakly compressible SPH under the DualSPHysics framework to simulate nonlinear wave propagation, Rota Roselli et al. [71] identified, in addition to N_{pH}, the smoothing length β_h and the artificial viscosity coefficient γ_v as important parameters for the accuracy of nonlinear wave propagation. β_h denotes the interaction range between particles during computation and impacts the accuracy and computational efficiency of the model. In the D-SPH model, $\beta_h = c_{hd_p}\sqrt{2}$ is applied. As shown by Padova et al. [70], high values of γ_v can lead to wave height underprediction, whereas very low values can lead to model instability. Preliminary sensitivity analyses of the smoothing length (by c_h) and artificial viscosity term were carried out with $c_h \in \{1.2,\ 1.5,\ 1.8\}$ and $\gamma_v \in \{0.01,\ 0.03,\ 0.05\}$. Qualitatively, the analyses showed only little influence on the surface elevation time series and to avoid tuning the D-SPH model, commonly used values for wave transformation cases with wave-breaking of $c_h = 1.8$ and $\gamma_v = 0.01$were deployed for all simulations [71, 72]. Resultantly, the convergence analysis of D-SPH focused on the variation of N_{pH} which was also identified as the most important SPH parameter for wave transformation over a shallow foreshore by Gruwez et al. [69]. The convergence analysis of D-SPH

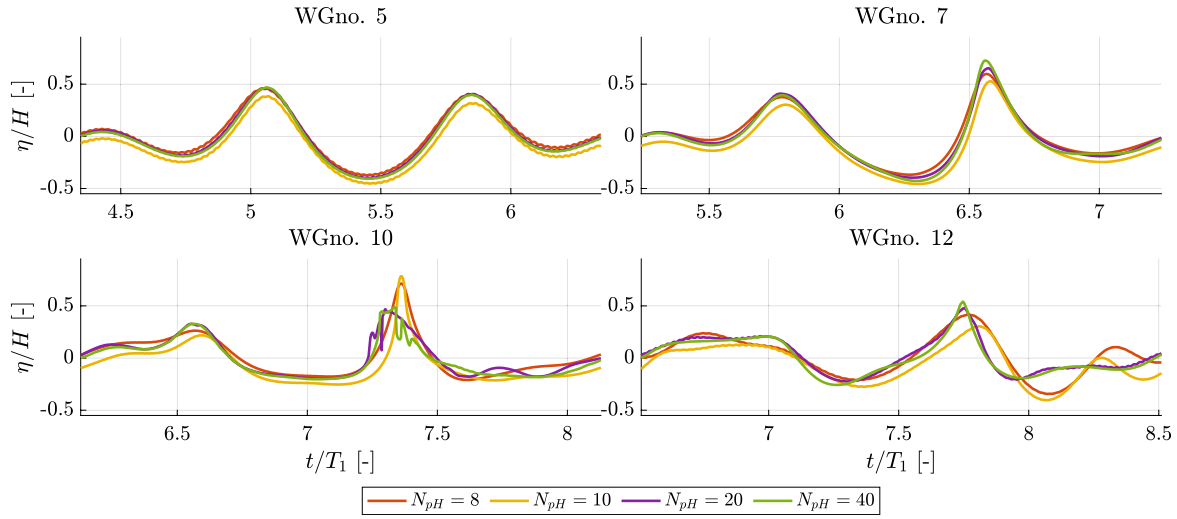

Fig. 16 Influence of N_{pH} on the surface elevation time series for selected WGnos.; wave condition 4

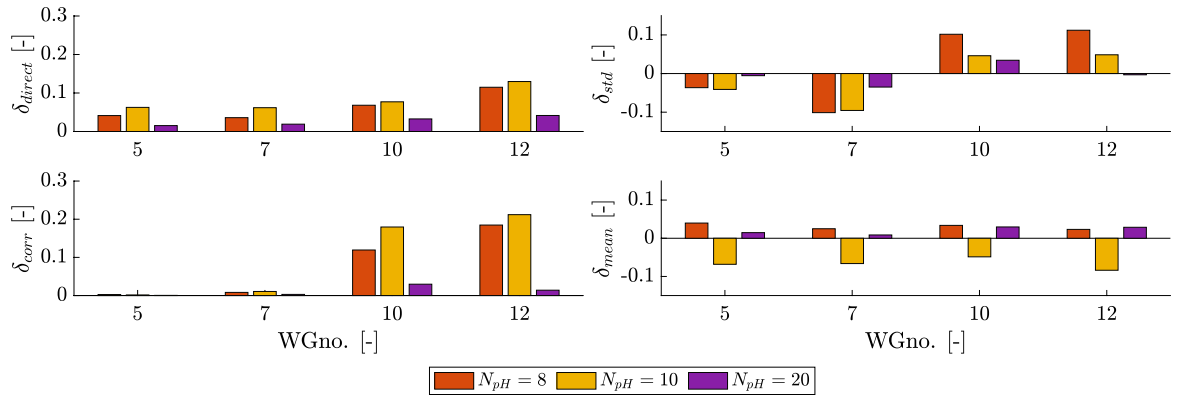

Fig. 17 Influence of N_{pH} on evaluation metrics for selected WGnos.; wave condition 4

was accordingly based on $N_{pH} \in \{8,\ 10,\ 20,\ 40\}$. The influence of N_{pH} for the selected surface elevation time series and evaluation metrics are shown in Figs. 16, 17. From the qualitive assessment of the surface elevation in the non-breaking region (WGnos. 5 and 7) wave profiles are rather similar for all N_{pH} except for a negative offset for $N_{pH} = 10$ yielding $\delta_{mean} < -5\%$ indicating a lower wave set-up for this spatial resolution. At WGnos. 10 and 12, where turbulent effects from wave-breaking are present, the influence on wave profiles from N_{pH} is significantly larger with large visible deviations at around $t/T_1 = 7.25$ and $\delta_{direct} > 10\%$ for $N_{pH} \leq 10$. Sufficient convergence is obtained with $N_{pH} \geq 20$ where all evaluation metrics are $< 5\%$ and only slight variations at the turbulent bore is visible from the surface elevation time series in Fig. 16.

Similar convergence analyses were carried out for the D-SPH model with wave conditions 1–3, see Figs. 53, 54, 55, 56, 57, 58 in Appendix A.3, with conclusions summed up in Table 9. It should be noted the convergence with N_{pH} was somewhat weak for namely the breaking wave condition 3, where small variations of d_p could lead to erratic changes of the surface elevations at the turbulent bore, as seen for WGnos. 10 and 12 in Figs. 57 and 58. Divergence was also identified when increasing the resolution further, i.e., to $N_{pH} \geq 40$, without varying multiple other parameters underlining the weak convergence of the D-SPH model with N_{pH} under the specified conditions. Despite the lack of formal convergence in wave condition 3, $N_{pH} = 40$ was used for further analysis and comparison as relatively good agreement were found between $N_{pH} = 20$ and $N_{pH} = 40$

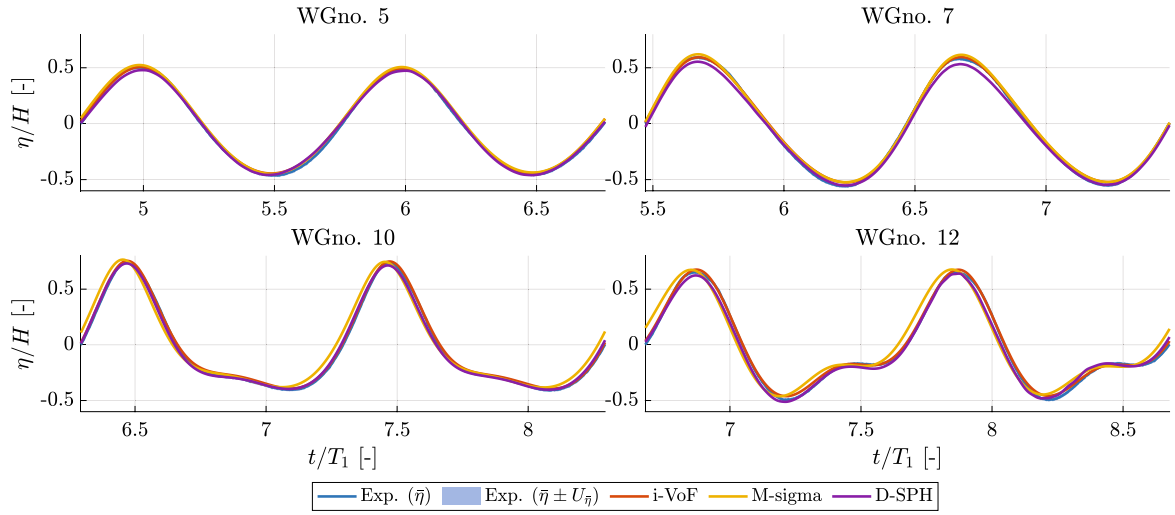

Fig. 18 Comparison of numerical models; surface elevation time series at selected WGnos. in wave condition 1

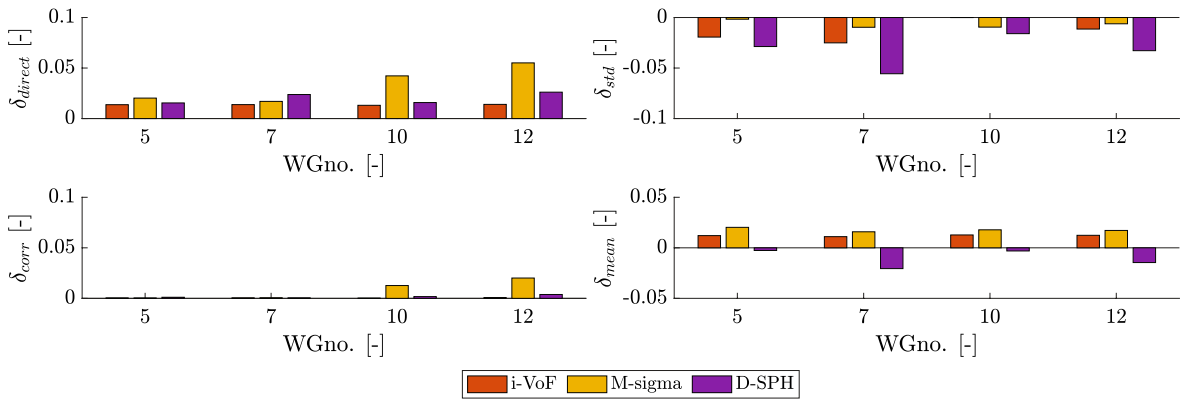

Fig. 19 Comparison of numerical models; evaluation metrics for selected WGnos. in wave condition 1

and these posed less erratic and more physically plausible than $N_{pH} = 60$ as interpreted from Figs. 57 and 58. The observed case-specific convergence is further discussed in Sect. 8.3.

The application of the weakly compressible SPH solver of the DualSPHysics framework is known to be prone to density fluctuations (and therefore pressure fluctuations as per the Tait equation) even with employment of the DDT of Fourtakas et al. [59]. In simulating virtually incompressible fluid flows with a weakly compressible solver it is important to ensure that the incompressibility conditions are nearly met aiding to mitigate said spurious density fluctuations. In the recent publication of Khayyer et al. [73] schemes for enhanced satisfaction of incompressibility conditions in weakly compressible SPH are presented which are planned to be included in future releases of DualSPHysics [74]. In the present study, such schemes were not deployed but the density field were monitored to not contain excessive variation or discontinuities. In Appendix B, the density field in the two breaking wave conditions 3 and 4 is shown to be continuous in the vast majority of the domain and vary with less than 1 % of the nominal (or initial) density over a wave period—as generally targeted with the weakly compressible SPH method, see, e.g., Khayyer et al. [73].

7 Results

The various numerical models and physical test results are compared in time domain qualitatively with surface elevation time series and quantitively with evaluation metrics at four selected wave gauges in Sect. 7.1. In Sect. 7.2, results are analyzed in frequency domain with calculation of amplitudes and phases of primary and higher-order harmonics along the *x*-coordinate of the wave flume. An inter-model comparison of the free surface representation of the

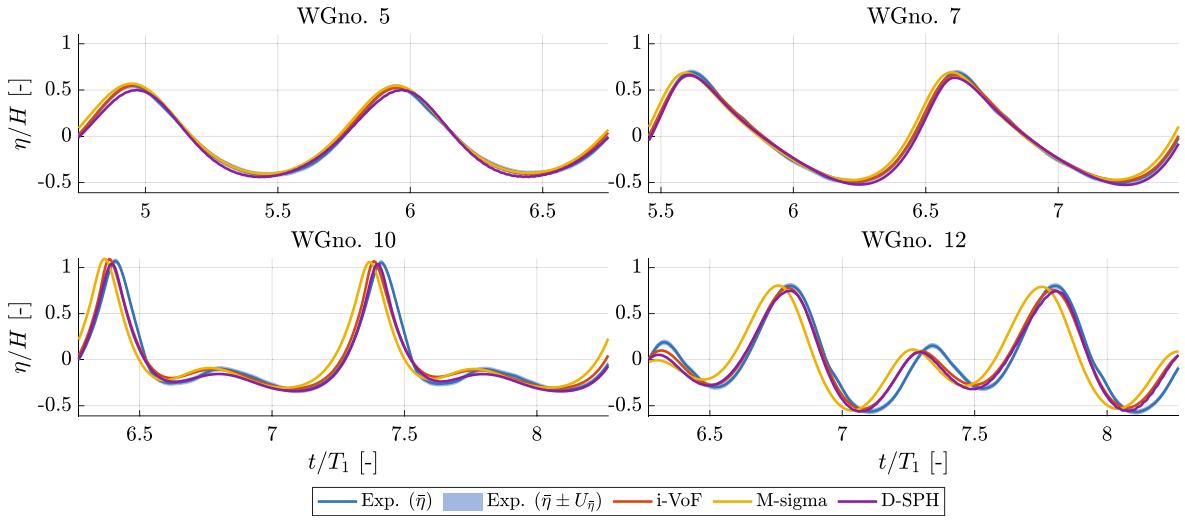

Fig. 20 Comparison of numerical models; surface elevation time series at selected WGnos. in wave condition 2

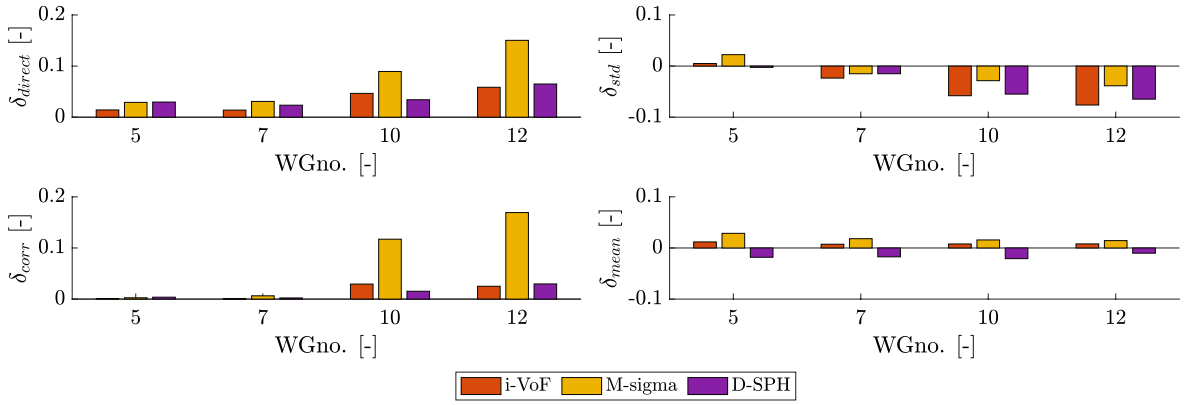

Fig. 21 Comparison of numerical models; evaluation metrics for selected WGnos. in wave condition 2

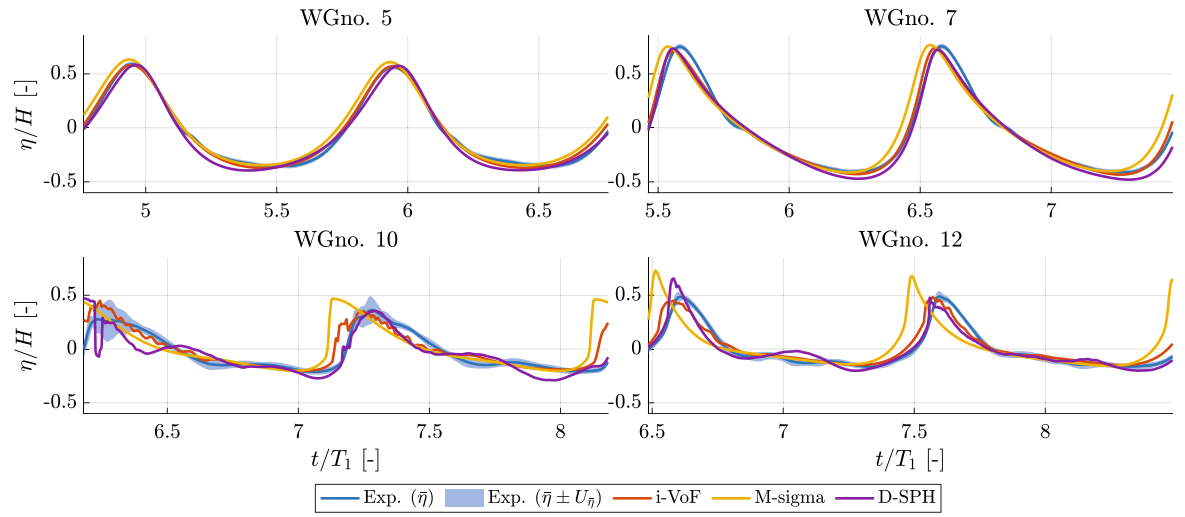

Fig. 22 Comparison of numerical models; surface elevation time series at selected WGnos. in wave condition 3

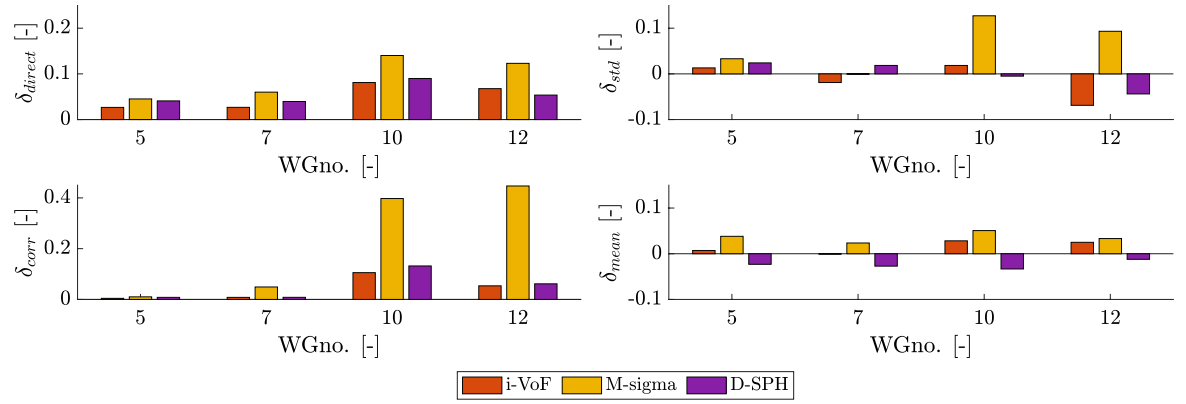

Fig. 23 Comparison of numerical models; evaluation metrics for selected WGnos. in wave condition 3

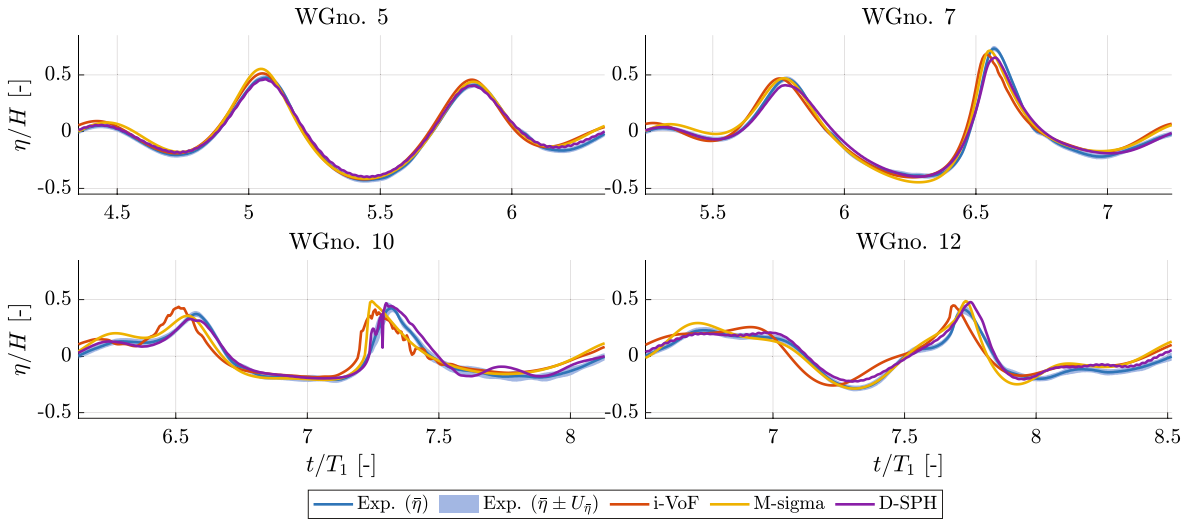

Fig. 24 Comparison of numerical models; surface elevation time series at selected WGnos. in wave condition 4

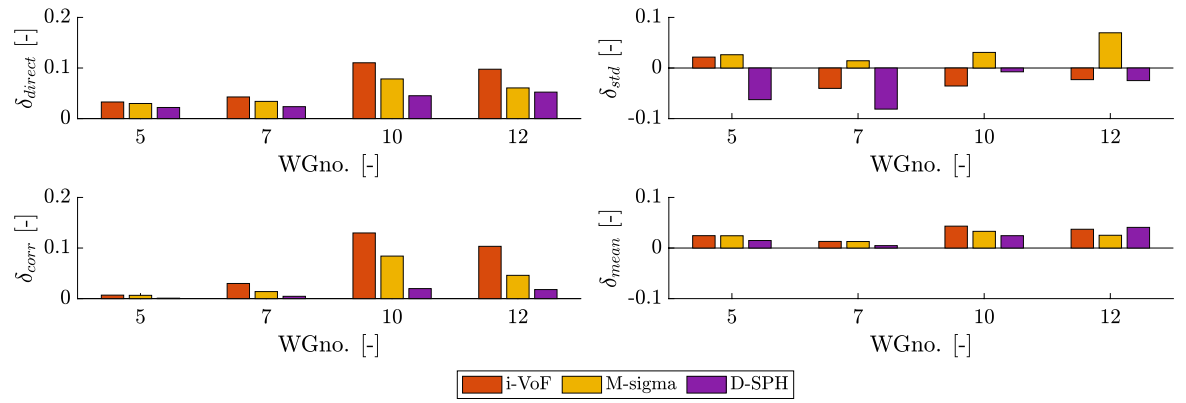

Fig. 25 Comparison of numerical models; evaluation metrics for selected WGnos. in wave condition 4

turbulent bore from wave-breaking is presented in Sect. 7.3. Ultimately, the computational costs of the numerical models are reported in Sect. 7.4. Results are interpreted and discussed in Sect. 8.

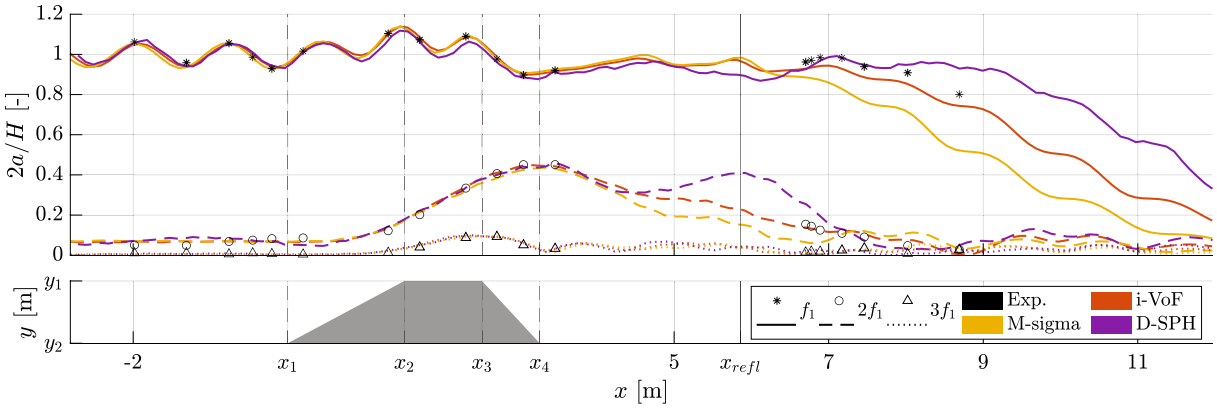

Fig. 26 Amplitude evolution along the wave flume; wave condition 1

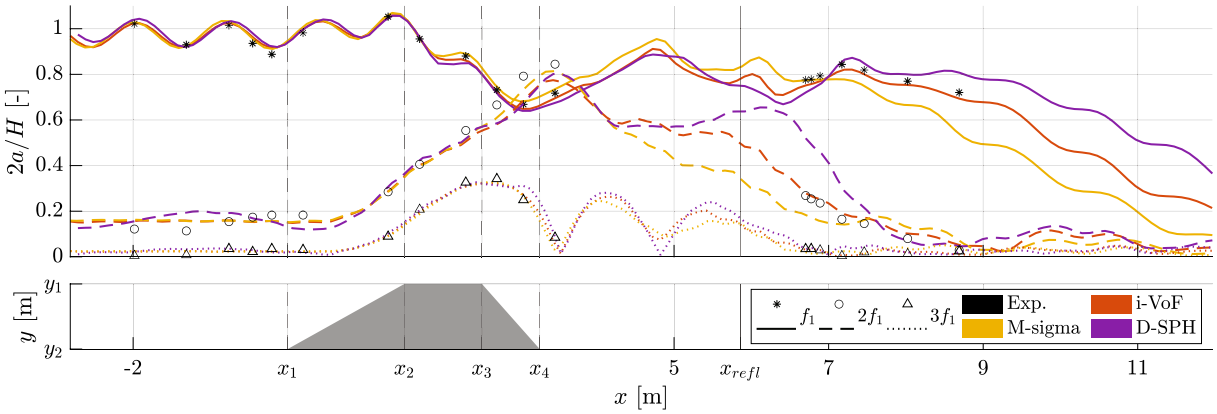

Fig. 27 Amplitude evolution along the wave flume; wave condition 2

All numerical surface elevation time series are aligned to the physical tests at WGno. 1 by maximizing the cross-correlation of the surface elevation time series over a time-window of $2T_1$ extracted from the second zero-up-crossing after wave propagation (estimated by L_1/T_1) to the position of WGno. 1. Prior to the alignment, signals were up-sampled to 1000 Hz by linear interpolation to obtain a higher precision in the alignment of the signals.

7.1 Time domain comparison

Surface elevation time series and derived evaluation metrics are extracted for the wave gauge positions also considered in the convergence analyses of Sect. 6, i.e., WGnos. 5, 7, 10, and 12, see Figs. 18, 19, 20, 21, 22, 23, 24, 25. Time series are extracted based on the second zero-up-crossing after wave propagation (estimated by L_1/T_1) to the wave gauge positions and wave-ramp-up of $2T_1$ based on the physical test results—thus revealing possible phase-shifts from the numerical models.

7.2 Frequency domain comparison

The amplitude a and phase θ of primary and higher-order harmonics were calculated from FFT analyses as a function of x. To this end, numerical models were employed with a high number of numerical wave gauges (150 equidistantly spaced in x) to attain smooth amplitude and phase curves from numerical results with discrete comparisons to physical test results at physical wave gauge positions. Phases were unwrapped and linearly upsampled to 1500 points in x and rewrapped in $[0;2\pi]$ radians to obtain proper sawtooth depictions of phase variation with x. The FFT analyses were carried out for time windows with lengths of $2T_1$. x_{refl} is the highest x-coordinate where the FFT analyses can be carried out from the physical test results without reflections from the passive absorption entering the analyses and with waves assessed

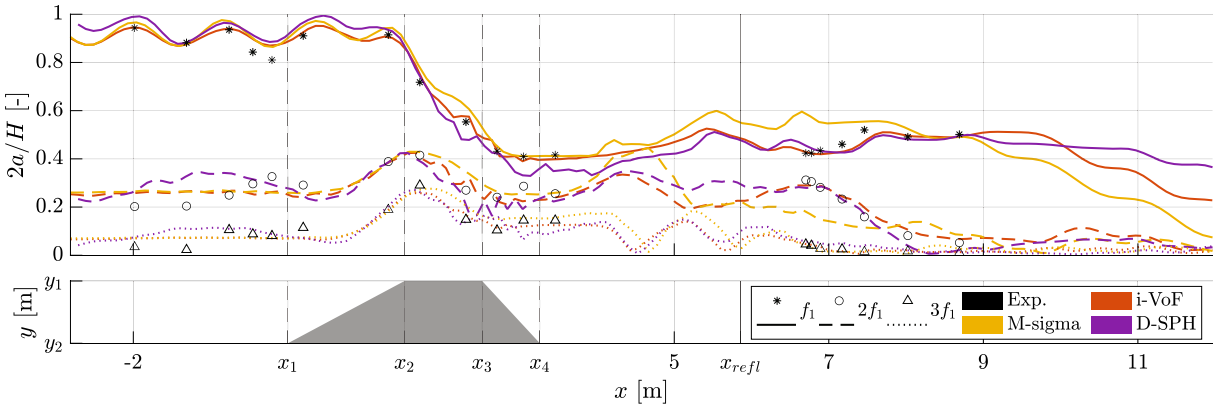

Fig. 28 Amplitude evolution along the wave flume; wave condition 3

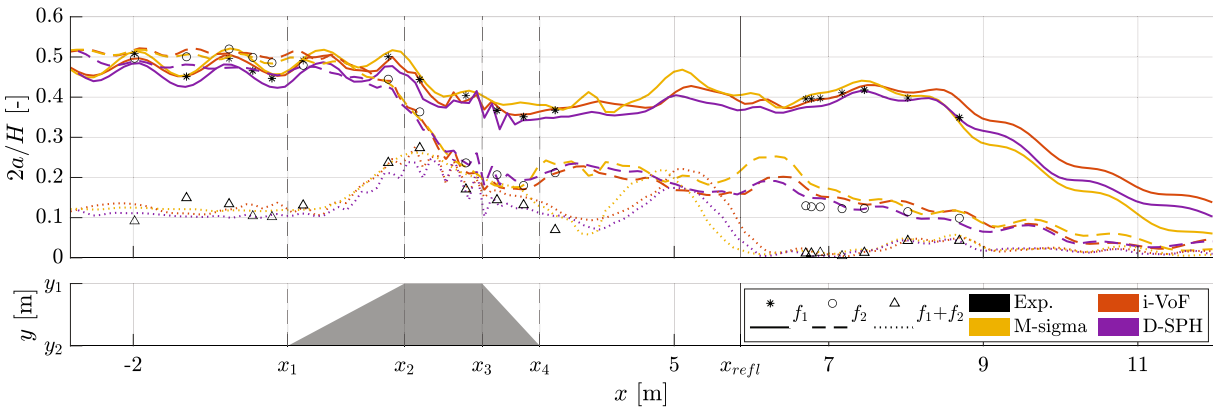

Fig. 29 Amplitude evolution along the wave flume; wave condition 4

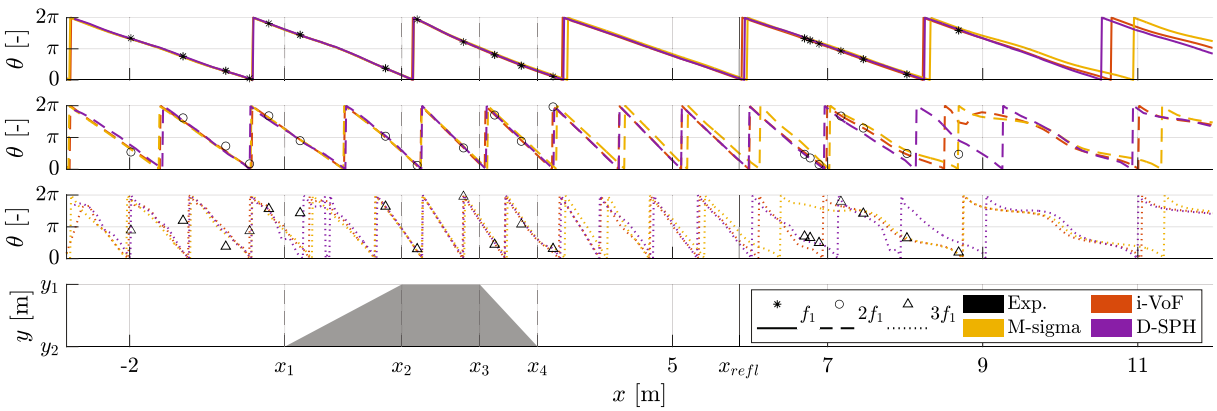

Fig. 30 Phase evolution along the wave flume; wave condition 1

fully developed (ramp-up of $2T_1$ and an additional T_1 to disregard the leading wave after ramp-up). As the extracted time window for the FFT is $2T_1$, $x_{refl} = x_5 - 5L_1/2$. Consequently, the time window begins at $t_{refl} = x_{refl}/(L_1/T_1) + 3T_1$ and ends at $t_{refl} + 2T_1$ where t_{refl} denotes the time just before reflection from the end of the flume reaches x_{refl}. Amplitudes and phases at f_1, $2f_1$, and $3f_1$ are calculated for the regular wave conditions 1–3, see 26, 27, 28 and 30, 31, 32, while the contents at f_1, f_2, and $f_1 + f_2$ are calculated for wave condition 4, see Figs. 29 and 33. The contents on $2f_1$, $2f_2$, and $f_2 - f_1$ in wave condition 4 are omitted due to brevity.

7.3 Inter-model comparison of turbulent bore

Free surface representations of the turbulent bore by the various numerical models are given in Figs. 34 and, 35 for wave condition 4 at time coordinates corresponding to the second zero-up-crossing at WGno. 10 in Fig. 24, i.e., $t/T_1 \approx 7.25$. The free surfaces are represented by the phase fraction field $\alpha = 0.5$ in the i-VoF model, the sigma coordinate $\sigma = 1$ (re-transformed into y-coordinates in Fig. 35) with the M-sigma model, and the mass limit of 0.4 in the D-SPH model.

7.4 Computational costs

In addition to the accuracies of the considered numerical models against the physical test results, which will be addressed in Sect. 8.2, the benchmarking will be based on the computational costs. Three different hardware setups of similar price range (and accessible to typical engineering companies or research facilities) were applied for the three different numerical models. Comparison of the wall clock times, with the respective hardware specifications in mind, will be the basis of the computational cost benchmark discussed in Sect. 8.3. A more clean comparison would utilize the exact same hardware setups across numerical models, but given the different requirements for operating systems and the possibility of GPU acceleration with DualSPHysics this was not feasible nor necessary for a gross inter-model comparison of computational costs in the present study.

All simulations with the i-VoF model were run in parallel on 30 cores on a single CPU (AMD EPYC 7702; base clock speed 2.0 GHz). The Scotch decomposition method [75] was employed to decompose the mesh into the 30 subdomains while minimizing connectivity. The number of computational points (cells) and wall clock time of the converged i-VoF simulations of each wave condition are shown in Table 10. It should be noted that the number of cells per core varies between 13e3 and 40e3 which typically is the interval in which strong scaling speed-up performance degenerates somewhat rapidly, see, e.g., [76].

The M-sigma model ran on 16 cores on a single AMD Ryzen 9 3950X CPU (base clock speed 3.5 GHz). Domain decomposition was carried out with the METIS graph partitioning library minimizing connectivity between subdomains on the allocated cores [77].

The D-SPH models were executed with an AMD 7302 CPU accelerated with the Tesla A10 GPU having 9216 CUDA-cores and single precision processing power of 31240 GFLOPS. The computational costs are summed up in Table 10.

8 Discussion

The wave transformation physics of the presented test case is discussed in Sect. 8.1 and will primarily be based on the physical test results but in the areas of the physical wave flume where wave gauges were not installed, conclusions are drawn from the numerical tests with dense numerical wave gauges. The numerical models are benchmarked against the physical tests in terms of accuracy in Sect. 8.2, while inter-model applicability is discussed in Sect. 8.3.

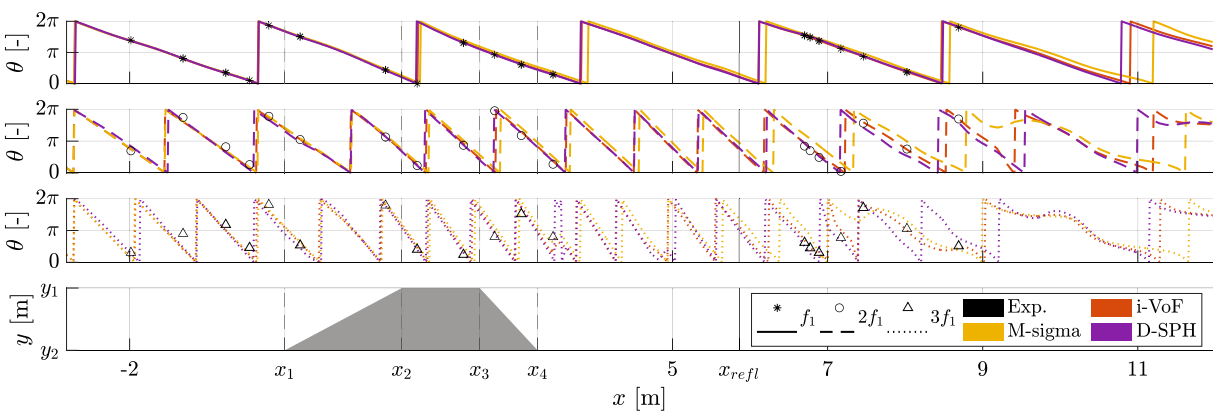

Fig. 31 Phase evolution along the wave flume; wave condition 2

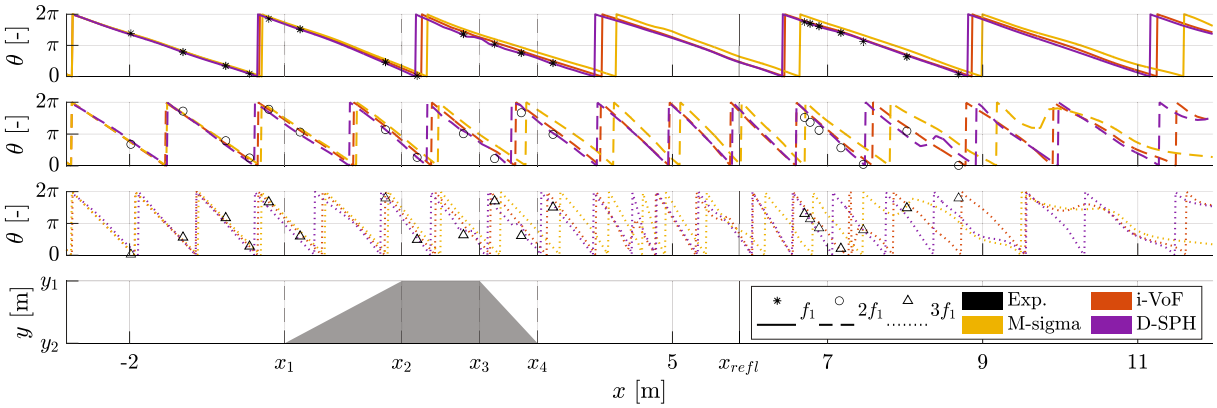

Fig. 32 Phase evolution along the wave flume; wave condition 3

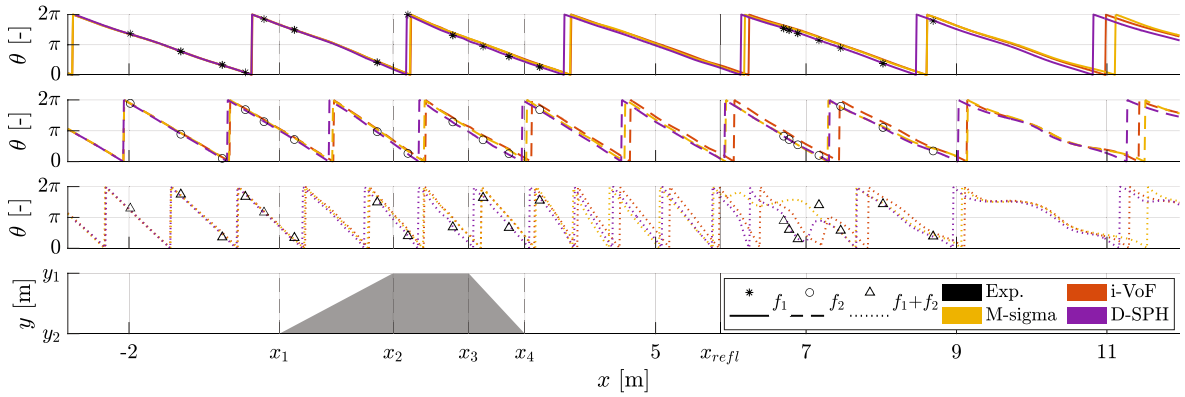

Fig. 33 Phase evolution along the wave flume; wave condition 4

8.1 Wave transformations

Upwave of the submerged bar, at $x < x_1$, symmetric wave profiles with increasing nonlinearity with wave condition number can be seen from the surface elevation time series in Figs. 18, 20, 22, and 24. The relative distribution of energy on primary components and their respective superharmonics are shown in Figs. 26, 27, 28, 29. From the numerical results on spatial evolution of phases in Figs. 30, 31, 32 the second and third order components from wave conditions 1–3 have wavelengths of half and one-third of that of the primary component, i.e., equal celerity, as expected for bound superharmonics. For wave condition 4, the primary components can be seen to have a wavelength ratio of about $L_1/L_2 = 1.7$ from Fig. 33 which approximately corresponds to the wavelength ratio as calculated from linear dispersion. The same holds for the superharmonic $f_1 + f_2$ which wavelength corresponds to $k_1 + k_2$ (additional super- and subharmonics are omitted due to brevity). At the upslope of the submerged bar, at $x_1 < x < x_2$, the shoaling process initiates, and the wave nonlinearity increases which can be seen from the increasing amplitudes with x on higher-order components in Figs. 26, 27, 28, 29. Consequently, skewness increases, and asymmetric wave profiles emerge, which is apparent from the surface elevation time series at WGno. 7 for all wave conditions (though only mildly for wave condition 1) as can be seen in Figs. 18, 20, 22, and 24. At the horizontal crest of the submerged bar, at $x_2 < x < x_3$, the re-adjustment to a horizontal bathymetry releases higher-order bound energy to symmetrize the asymmetric incident wave profiles. This effect is significant for large changes in the bathymetry slopes, see Eldrup and Lykke Andersen [78] The h/L_1 ratio is around the conventional shallow-water limit of 5% and waves in this region are accordingly rather non-dispersive. The near-resonant conditions of triad wave-wave interactions are met [79] which yields a rapid transfer of energy from primary to higher-order harmonics. For the non-breaking wave conditions 1 and 2 this exchange of energy is clearly seen from significant increases in second and third order energy (third order mainly in wave condition 2), see Figs. 26 and 27. Interestingly, for the breaking wave conditions 3 and

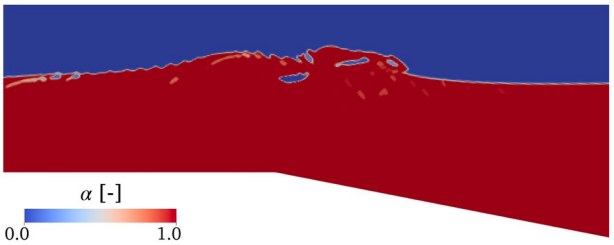

Fig. 34 Free surface of the i-VoF model at $t/T_1 = 7.20$

Fig. 35 Free surface of the M-sigma model at $t/T_1 = 7.22$ with the sigma domain (red) seen in Cartesian coordinates

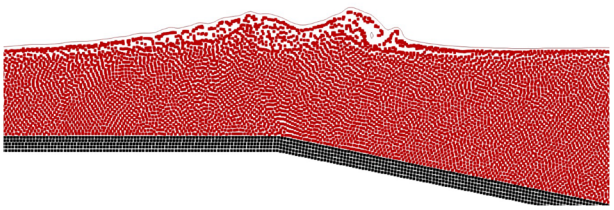

Fig. 36 Free surface of the D-SPH model at $t/T_1 = 7.24$ with fluid particles in red and boundary particles in black

4, dissipation seems to be the dominant wave transformation rather than triad wave-wave interaction. Dissipation by the formation of turbulent eddies from the onset of wave-breaking and the development of a turbulent bore is apparent from the significant reduction of energy on virtually all harmonics with the dissipation of primary energy being larger on f_2 than f_1 in wave condition 4 as expected due to the higher wave-steepness of f_2, see Figs. 28 and 29. From the variation of phases with x, the celerity at the horizontal bar crest decreases less for the relatively higher amplitude wave conditions indicating amplitude dispersion and thus the relatively higher nonlinearity in these wave conditions. At the downslope and downwave of the submerged bar, at $x > x_4$, the finite amplitude waves from the horizontal bar crest propagate into deeper water and the wave nonlinearity decreases and energy is transferred between components. With sufficiently high downslopes energy will not solely be transferred from higher-order bound components to primary components, i.e., deshoaling is not simply the inverse of shoaling, but a decomposition into free harmonics with smaller amplitudes occur as found by Beji and Battjes [4] and Eldrup and Andersen

Table 10 Computational cost of the considered numerical models

Wave condition	Comp. point count [-]	Wall clock time [h]	Hardware
i-VoF			
1	0.4e6	0.5	
3	0.7e6	17.2	30 CPU-c.
2	0.6e6	2.4	(2.0 GHz)
4	1.2e6	23.0	
M-sigma			
1	0.4e4	0.01	
3	3.1e4	0.16	16 CPU-c.
2	0.7e4	0.02	(3.5 GHz)
4	3.1e4	0.14	
D-SPH			
1	3.5e6	12.6	
2	0.7e6	1.9	9216
3	0.8e6	3.6	CUDA-c.
4	0.2e6	1.4	

'c.' denotes cores

[78] for downslopes of 1:10 and 1:30, respectively. The oscillating amplitudes in space as seen particularly for the second- and third-order harmonics of wave conditions 2 and 3 are characteristic of this exact phenomenon [78] which comply with the steeper downslope of 1:5 in the presented tests, see Figs. 27 and 28. For multiple wavelengths, the exchange of energy transpires, and ultimately a steady state will develop, assuming a continued flat bathymetry [80]. Such a steady state is not reached in the analyzed domain of the presented tests.

8.2 Accuracy of the numerical models

Close agreement between the numerical models and the physical tests resides in the prediction of the spatial evolution of amplitude on both primary and higher order components (if present) with no numerical model clearly standing out from the rest, see Figs. 26, 27, 28, 29. The overall transfer of energy between components as attained from the physical tests is very well captured by the numerical models along the domain with deviations increasing at about midway of x_3 and x_{refl} ($x \approx 4$ m, particularly clear from Figs. 26 and 27. At $x > x_{refl}$ reflections and transients due to ramp-up enter the FFT analyses. However, released higher order harmonics from transients due to ramp-up enter the FFT analyses upwave of this region due to their lower celerity, i.e., a released component on $2f_1$ from the first wave after ramp-up will enter analyses at about $x > 4$ m. Since various ramp-up formulations are used in the numerical models the largest inter-model deviations are present in this region wherefore $x > 4$ is not taking into account in the assessment of model accuracy but is sustained in the results for completeness. It should be noted that the physical tests now pose as the reference for evaluation metrics as introduced in Sect. 5.

The M-sigma model have the highest direct errors in wave conditions 1–3 which is driven by phase shifts increasing with nonlinearity, i.e., $\delta_{corr} = [2, 12, 40]\%$ at WGno. 10 for wave condition 1–3, respectively. The phase shifts primarily develop at the horizontal crest of the submerged bar as seen in Figs. 30, 31, 32, where the celerity of M-sigma can be seen to be overestimated in both primary and higher order harmonics for wave conditions 1–3. Interestingly, in wave condition 4, δ_{corr} for M-sigma is reduced to 9% where that of i-VoF is maximum with 13% resulting in the largest direct error in wave condition 4. This is the highest evaluation metric for i-VoF which remains consistently accurate in both the general shape of the surface elevation time series and crest and trough elevations throughout all wave conditions. D-SPH and M-sigma have considerable overestimations on maximum crest elevations with deviations of 30% and 38%, respectively, relative to the upper bound of the 95% UI, whereas i-VoF lies within the UI.

Considering the spatial evolution of amplitudes in the nonbreaking wave conditions 1–2, see Figs. 26 and 27, the largest deviations are on the second order energy at deshoaling, $x_3 < x < x_4$. The amplitudes on f_1 are predicted with deviations of less than 5% for all numerical models in this region while the amplitude on $2f_1$, which has increased to be of equal magnitude to that of f_1, is generally less accurately captured. Slightly higher accuracy is obtained with the M-sigma model having a maximum deviation of 10% where i-VoF and D-SPH have 15%. The amplitudes on $3f_3$ match the physical tests with maximum deviations of 5% with i-VoF and M-sigma while D-SPH has an overestimation at WGno. 11 seemingly due to a delay in the decomposition process, but otherwise correlates well with i-VoF and M-sigma.

The inter-model variability of the predicted amplitudes generally increases with increasing nonlinearity of the considered wave condition with additional variability introduced in the breaking wave conditions 3 and 4. The turbulent bore generated from wave breaking at the horizontal bar crest and measured from surface elevations at WGno. 10 (Figs. 22 and 24) is, not surprisingly, found to contain some of the most challenging physical processes from a modelling perspective, as also seen in the convergence analyses in Sect. 6. It is largely in this region of the domain the characteristics of the tested numerical models with their different free surface treatments manifest as underpinned from the free surface representations in Figs. 34, 35, 36: in the i-VoF model, the turbulent bore is simulated with a complex free surface with air entrainments from plunging, and oscillations are transpiring at the interface; the M-sigma model develops a steep, nearly vertical bore-front activating turbulent dissipation while maintaining a continuous, single-valued free surface as per the sigma transformation method; while the D-SPH model simulates a bore with complex free surface deformations with particle clustering and particle voids forming at the vicinity of the free surface which can result in sudden drops in the extracted surface elevation time series, as seen for $t/T_1 = 7.29$ at WGno. 10 in Fig. 24. In case of multi-valued free surfaces, the lowest value was extracted as surface elevation in D-SPH whereas in i-VoF the highest value was extracted (due to the inclusion of air entrainment). The definition of the surface elevation with resistance wave gauges is unclear at multi-valued free surfaces which is most pronounced in the present testcase with the plunging waves in wave conditions 3 and 4. However, the effect from different definitions of the surface elevation in numerical models and physical tests is assessed to be small in the present benchmarking where the surface elevations of plunging waves are not included directly, i.e., wave gauges were not installed in the physical tests to measure the plunging waves but rather the evolution of the surface elevation including the turbulent bore downwave hereof.

The dissipation from wave-breaking in the M-sigma model does not fall short of the i-VoF and D-SPH models where full free surface deformations are possible, see Figs. 28 and 29. In the dissipative region of $x_2 < x < x_4$, the numerical models generally comply with the physical test data points relative to which the largest deviations are 10% for all numerical models on the primary components in wave condition 4 and 19%, 11%, and 5% for D-SPH, M-sigma, and i-VoF, respectively, in wave condition 3. The corresponding deviations with reference to H/2 rather than the individual amplitudes (which is somewhat small for higher order components) are $2-5\%$ in wave condition 4 and 6%, 8%, and 3% in wave condition 3. i-VoF is thus the most accurate model with respect to turbulent dissipation while all the numerical models perform rather accurately with deviations of less than 10% of $H/2$ on the prediction of amplitudes during breaking on all components—abundant for most practical engineering.

For all wave conditions the generated waves correlate well between numerical models and physical tests as seen from the surface elevation time series at WGno. 5 with evaluation metrics generally low (most are below 5%), see Figs. 18, 19, 20, 21, 22, 23, 24, 25. Most notably at $x < x_1$ is the underestimation of the energy content in wave condition 4 with the D-SPH model yielding $\delta_{std} = 6\%$ which also can be seen as the slight negative offset in the amplitude on f_1 in Fig. 29. The influence hereof is mitigated at wave-breaking whereafter D-SPH obtain the overall lowest evaluation metrics and has a profile very close to the those of the physical tests at the challenging WGnos. 10 and 12, see Figs. 24 and 25. In wave conditions 2 and 3 variations in the amplitudes upwave of the submerged bar, $x < x_1$, are present, see Figs. 27 and 28. The primary amplitudes from the physical test results differ locally in x (just upwave of $x = x_1$) with about 10% from all numerical models whose inter-model variability is very low. This could signify that the physical tests do not perfectly match the idealized test case, e.g., from geometrical imperfections or structural flexibility of the bar. Additionally, higher order components at $x < x_1$ obtained from D-SPH and the physical tests differ somewhat from one another and from i-VoF and M-sigma which are nearly equal and constant. Re-reflections are mitigated in the i-VoF and M-sigma models which utilize the relaxation zone technique at the inlet whereas D-SPH and the physical tests utilize piston motion with distinctive wavemaker theories. The effects hereof, besides general differences in the model/physical test behavior, are expected to cause the deviations in second order energy upwave of the bar in wave conditions 2 and 3 which impact in the context of the dominating wave transformation of shoaling, breaking, and decomposition are assessed insignificant.

The authors acknowledge that the inclusion of pressure, turbulence characteristics, and/or velocity profiles as measurands could have increased the quality of the comparative analysis further - though also not included in the original paper of Beji & Battjes [4]. However, such enhancements would have increased the expenditures and complexity of the physical tests significantly are deferred for future investigation.

8.3 Applicability of the numerical models

Different hardware was used for the numerical models as presented in Sect. 7.4. The D-SPH model was accelerated with a GPU. The CPU for M-sigma had a significantly higher base clock speed relative to that used for i-VoF, that is, 3.5 and 2.0 GHz, respectively. On the other hand, i-VoF was parallelized to about the double number of cores than M-sigma was. The wall clock time on the M-sigma model was one to two orders of magnitude smaller than those of i-VoF and D-SPH regardless of wave condition, see Table 10. This significant reduction in simulation time is led by the sigma transformation approach from which the free surface is not resolved in the vertical direction as in i-VoF and D-SPH yielding substantial reductions in the computational point counts of the M-sigma model. The total computational point counts of i-VoF is two orders of magnitudes higher than those of M-sigma for each wave condition which decreases the timestep due to the imposed maximum C_{FL} criterion where the C_{FL} bounds in themselves are also significantly lower in i-VoF, see Table 7. Similar to i-VoF, the D-SPH model varies with orders of magnitude in the total computational point count relative to M-sigma, but somewhat contra intuitive the total computational point count in D-SPH decreases with increasing nonlinearity of the wave condition opposite of i-VoF and M-sigma. With constant normalized particle resolutions of $N_{pH} = 20$ for wave conditions 1, 2, and 4 and $N_{pH} = 40$ for wave condition 3, the simulation of small-amplitude waves requires higher absolute particle resolutions which upon initialization is uniformly scattered in the entire domain and not restricted to the vicinity of the free surface due to the lack of refinement zone options in D-SPH. These are significantly more challenging to implement in Lagrangian frameworks than Eulerian and the i-VoF model use local mesh refinement extensively and have parameterized mesh refinement zones by H from which computational point counts can be reduced significantly with decreasing nonlinearity. The i-VoF model is based on a structured mesh generated with OpenFOAM utilities which obviously introduces the inconvenience of the user having to design such—not required with the meshless D-SPH model or automatically generated with the M-sigma model (equidistant spacing in x and sigma is simply selected). However, for the utilized meshes with the i-VoF model this task is simple and should not last more than a few hours even for users with limited experience with OpenFOAM.

The M-sigma and i-VoF models converged with increasing resolutions in time and space to evaluation metrics well below 5% consistently across all wave conditions whereas the D-SPH model showed divergence with increasing N_{pH} in wave condition 3 and somewhat erratic behavior with small variations of d_p in the breaking wave conditions, see Sect. 6.3 and Appendix A.3. Convergence has been identified as a grand challenge of the SPH method [34] since currently convergence is not guaranteed by reducing smoothing and discretization errors by variation of the smoothing length and initial particle spacing but can dependent critically on the particle distributions and hence the flow field itself due to its Lagrangian formulation [81]. As the particle distribution can play a pivotal role in the accuracy of SPH it is presumed that the chaotic nature of turbulence in the breaking wave conditions triggers particle disordering yielding the observed erratic behavior. Despite the lack of formal convergence, the SPH method has a wide range of successful coastal engineering applications and in the present test case the D-SPH model accurately simulates wave transformation across the investigated wave conditions. However, relative to M-sigma and i-VoF more caution should be exercised in the convergence analysis of D-SPH as particle disordering may govern the accuracy which poses as a drawback of the model. Further work may include the influence from particle redistribution methods such as particle shifting to increase convergence and consistency as, e.g., considered by Vacondio [82] and Khayyer [83].

The free surface descriptions of i-VoF and D-SPH allow for straightforward advancement of the numerical models to include wave-structure interactions from, e.g., installation of a vertical crown wall at the submerged bar crest, from which the free surface is made discontinuous, and the sigma transformation accordingly breaks down without implementation of special measures such as artificial interior free surfaces as in [28]. The M-sigma model further has the disadvantage of not being based on an open-source code, unlike DualSPHysics and OpenFOAM, therefore not allowing for users to implement any such measures.

Numerical wave generation was most easily handled in i-VoF where no inputs other than the parameters given in the idealized test case were required as inputs across all wave conditions. The i-VoF and M-sigma models both utilized relaxation zone techniques of weighting analytical stream function wave theory solutions to computational fields accommodating undemanding wave generation of regular waves without restrictions on wave steepness. In D-SPH the standard wavemaker theory used with the piston wavemaker was second order [62] introducing generation of spurious free waves at too high wave steepness or for intermediate- to shallow-water waves, which could introduce deviations for D-SPH in the presently investigated wave condition 3. However, the second order wavemaker theory was maintained for all regular wave cases as the use of standard options within the respective numerical frameworks were pursued. Second order bichromatic wave theory was used as target solution in the inlet relaxation zone in the i-VoF model and the user needs only input wave parameters for the two primary wave components to generate the full wave-wave interactions. More work (and experience) was required in the D-SPH and M-sigma to generate wave condition 4. Irregular wave generation from bichromatic or user-defined spectra is not supported in current releases of D-SPH (first order irregular wave generation from JONSWAP or Pierson-Moskowitz spectra is). Therefore, wave condition 4 was generated from an input file with prescribed motion of the piston-type wavemaker calculated from external software through irregular second order wave maker theory of Schäffer [41]. In MIKE 3 Waves FM, the user can specify an input file with wave parameters for any number of wave components. Wave generation in M-sigma was thus initiated from an input file with amplitudes, periods, wavenumbers, and phases for all wave components (including interactions) in wave condition 4. An additional calculation was thus required to obtain the amplitudes of all wave components based on the two wave heights provided in the idealized test case. For this purpose, second order wavemaker theory as per [41] was used.

9 Conclusions

The wave transformation over a submerged bar was investigated for four wave conditions with various levels of nonlinearity, regularity, and turbulence due to wave-breaking. Physical wave flume tests were carried out to generate a dataset dedicated to numerical model validation. Three fundamentally different CFD models highly popular within their respective category were benchmarked against the physical tests in terms of accuracy while inter-model applicability in terms of computational cost and ease-of-use was discussed.

In general, the numerical models had high correlation with the physical tests with very low inter-model variability for especially the nonlinear, non-breaking wave transformations in wave conditions 1 and 2.

9.1 Conclusions on accuracy

Accuracy of the numerical models was assessed with reference to the physical tests from direct comparisons of surface elevation time series and derived evaluation metrics, indicating averaged errors on elevations, amplitudes, phases, and wave set-up, respectively, at multiple positions and the spatial evolution of amplitudes and phases on primary and higher order components.

Considering accuracy alone, the i-VoF model was found to have some advantages over D-SPH and M-sigma in primarily breaking wave conditions. Energy dissipation from turbulent bores formed from wave-breaking was captured with less than 5% deviation on primary amplitudes where those of M-sigma and D-SPH were 11% and 19%, respectively. As a possible effect from these deviations, D-SPH and M-sigma significantly overestimate maximum crest elevations downwave of the submerged bar where i-VoF lies within the 95% UI of the physical test results. Namely in wave condition 3, the wave celerity in the M-sigma model is overestimated at the horizontal crest of the bar resulting in rather large phase shifts of surface elevation time series and correlation errors downwave of the bar. D-SPH had the overall smallest phase shift errors. The highlighted deviations might seem somewhat minor in the context of the overall wave transformation from wave propagation over a submerged bar as seen from the spatial evolution of amplitudes along the wave flume (Figs. 26, 27, 28, 29) but may turn critical in delicate design situations based on, e.g., maximum crest elevations at a given position.

9.2 Conclusions on cost-accuracy trade-off

In terms of the cost-accuracy trade-off of the numerical models, the M-sigma performed the best with computational costs between one and two orders of magnitude lower than D-SPH and i-VoF as measured from wall clock time (see Sects. 7.4 and 8.3) with the nearly linear wave condition 1 being solved in close to real-time. The significant reduction in computational cost of the M-sigma model was led by the sigma transformation of the vertical coordinate reducing computational point counts two orders of magnitude relative to D-SPH and i-VoF and the knock-on effect of larger time steps from maximum CFL criteria. The accuracy of M-sigma followed that of D-SPH and i-VoF for the non-breaking wave conditions whereas for the breaking wave conditions accuracy were lower than i-VoF but generally higher than D-SPH. In wave condition 3, wave celerity at the horizontal bar crest is overestimated and the maximum wave crest elevations were overestimated at a position downwave of the bar, however, the energy dissipation as reflected by evolution of amplitudes from spectral analysis were generally well captured with an accuracy adequate for most coastal engineering applications.

9.3 Conclusions on applicability

An important caveat of the D-SPH model is the significantly more challenging task of obtaining converged results for especially breaking wave conditions compared to i-VoF and M-sigma. Convergence of SPH methods is an ongoing research topic and may depend critically on particle disordering [82], which is particularly unfortunate in the simulation of turbulent regions with a Lagrangian framework. In the present work, similar convergence criteria were retained in D-SPH as with i-VoF and M-sigma for all wave conditions except wave condition 3 which diverged with decreased initial particle spacing. The meshless nature of D-SPH and the automatically generated, simple meshes in sigma domain in M-sigma gives these models a slight edge over i-VoF in time spent on model setup. Advancement of the numerical models to handle more complex wave-structure interactions such as surface piercing structures like a crown wall may be more easily implemented in i-VoF and D-SPH than M-sigma due to their free surface descriptions and the open-source accessibility of the OpenFOAM and DualSPHysics.

Acknowledgements This work has received funding from the European Union's Horizon 2020 research and innovation program under the Marie Sklodowska-Curie Actions Grant agreement no. 101068736.

Author contributions J.A. and G.V.F. carried out the literature review, formulated the research questions, and organized the research. F.F. carried out the physical wave flume experiments. J.A. executed the numerical modeling with OpenFOAM (i-VoF), G.V.F. with SPH (D-SPH), and M.R.E. for Mike 3 Waves (M-sigma). Data analysis and interpretation were planned and undertaken by J.A. The original draft was written by J.A. All authors reviewed the paper.

Funding Open Access funding enabled and organized by Projekt DEAL. This work has received funding from the European Union's Horizon 2020 research and innovation program under the Marie Sklodowska-Curie Actions Grant agreement no. 101068736.

Data availability To encourage further numerical model benchmarking or validation against the experimental data of the present paper, datasets with results from the physical flume tests and numerical simulations are provided through the Zenodo repository of Andersen et al. [39]. This repository further contains the input files for all numerical models to increase transparency and reproducibility.

Declarations

Ethics approval and consent to participate This article does not contain any studies with human participants or animals performed by any of the authors.

Consent for publication Not applicable.

Competing interests The authors declare that they have no Conflict of interest.

Appendix A Convergence Analyses

The convergence analyses of wave conditions 1–3 are provided in the present appendix. Refer to Sect. 6 for the description of the convergence criteria and the convergence analyses of wave condition 4.

A.1 Convergence of i-VoF (wave conditions 1–3)

The convergence of wave condition 1 with N_{cH} can be seen in Figs. 37 and 38, and the convergence of wave condition 2 with N_{cH} can be seen in Figs. 39 and 40. With wave conditions 1 and 2, for maximum C_{FL} above 0.5 and 0.4, respectively, instabilities in the simulations arose. Variation of the maximum C_{FL} below these values yielded only very small differences in the surface evaluation time series with evaluation metrics smaller than 1% (the nature of which is discussed in Sect. 6); these figures have therefore been omitted. The convergence of wave condition 3 with N_{cH} can be seen in Figs. 41 and 42 while the convergence with the maximum C_{FL} can be seen in Figs. 43 and 44.

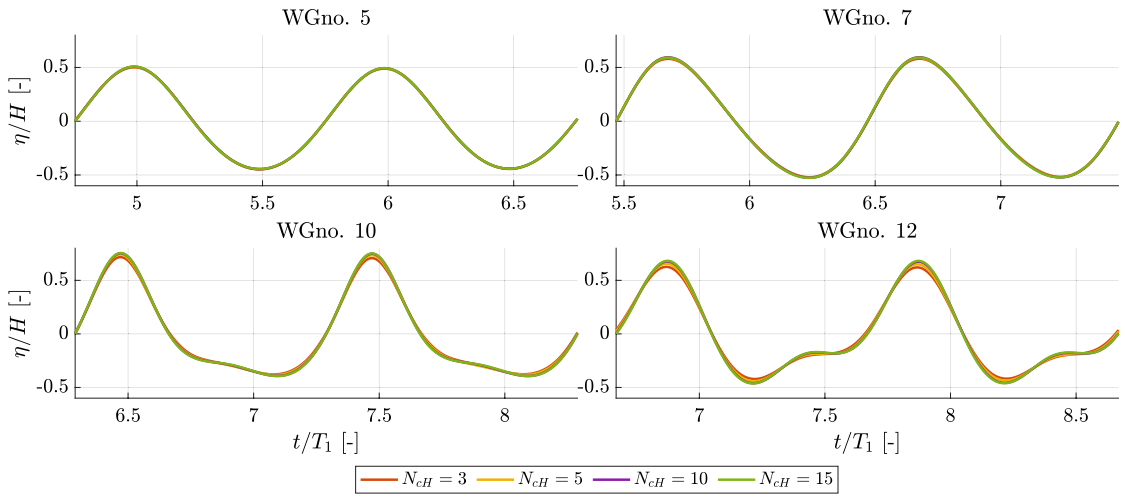

Fig. 37 Influence of N_{cH} on surface elevation time series for selected WGnos.; wave condition 1 and maximum $C_{FL} = 0.50$

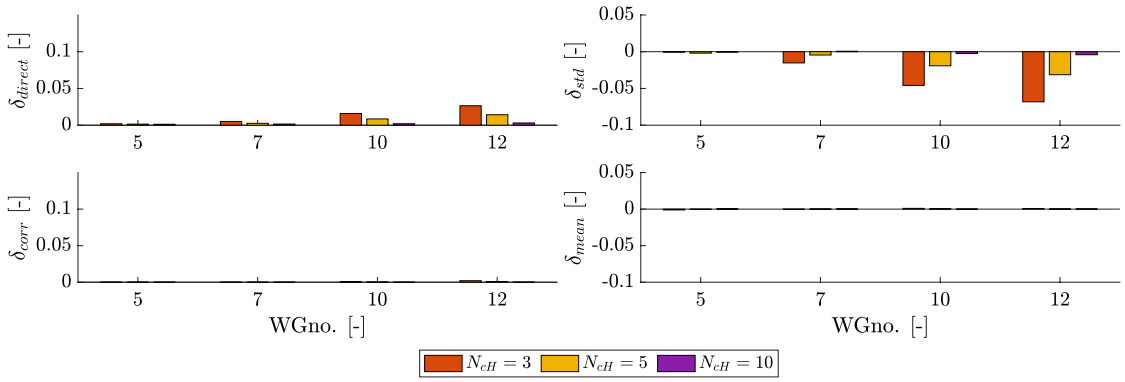

Fig. 38 Influence of N_{cH} on evaluation metrics for selected WGnos.; wave condition 1 and maximum $C_{FL} = 0.50$

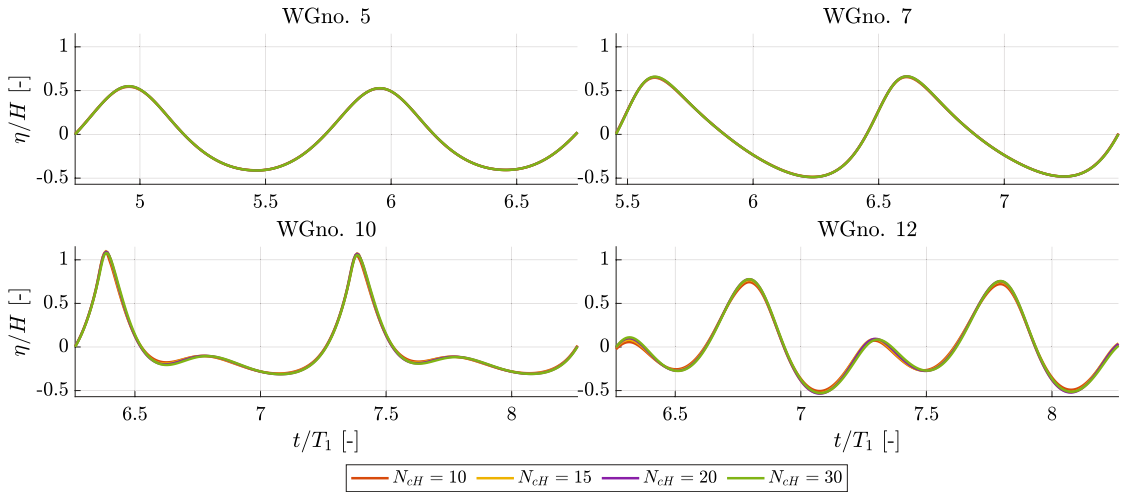

Fig. 39 Influence of N_{cH} on surface elevation time series for selected WGnos.; wave condition 2 and maximum $C_{FL} = 0.40$

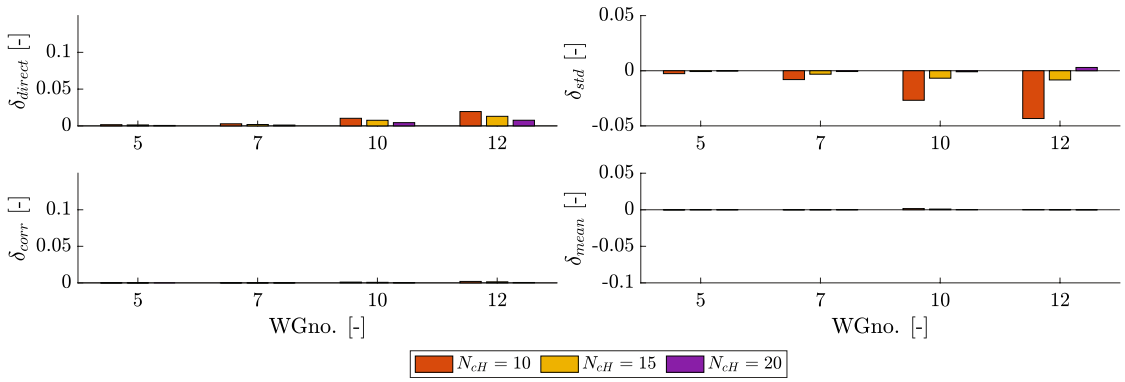

Fig. 40 Influence of N_{cH} on evaluation metrics for selected WGnos.; wave condition 2 and maximum $C_{FL} = 0.40$

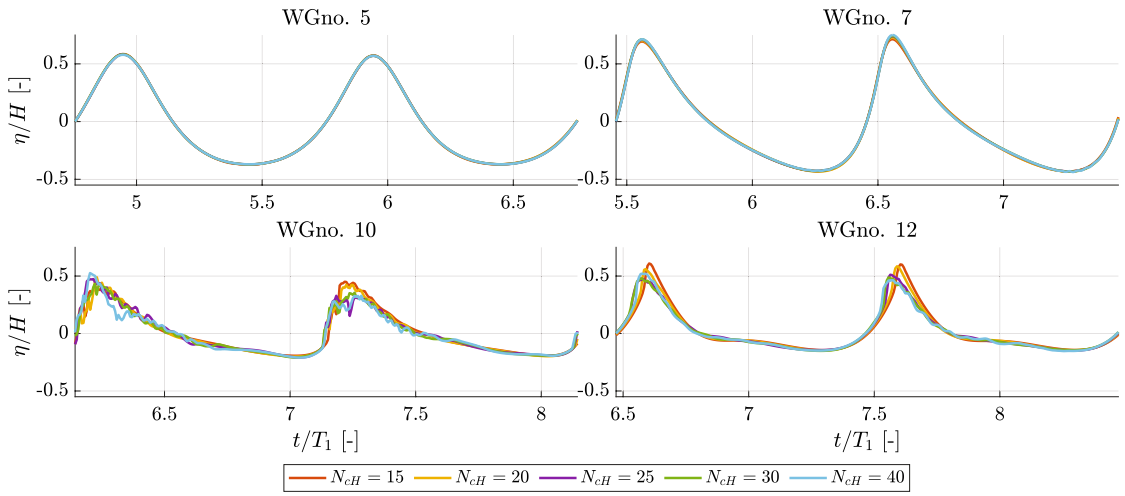

Fig. 41 Influence of N_{cH} on surface elevation time series for selected WGnos.; wave condition 3 and maximum $C_{FL} = 0.10$

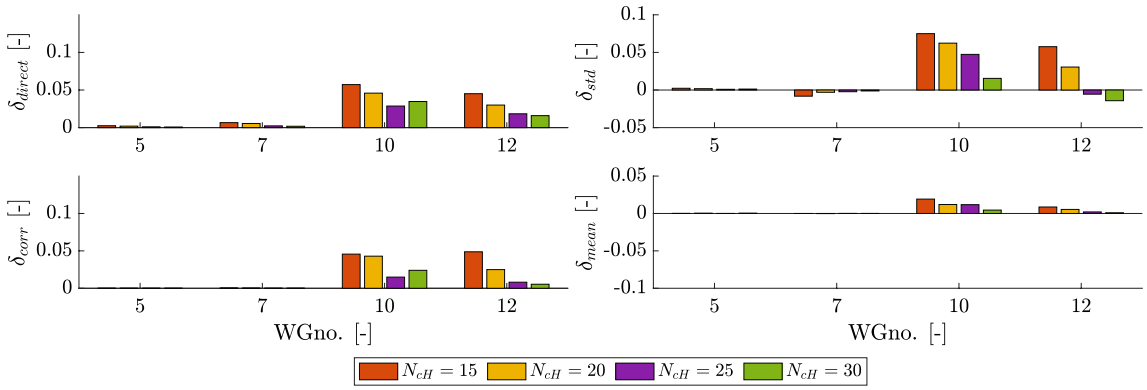

Fig. 42 Influence of N_{cH} on evaluation metrics for selected WGnos.; wave condition 3 and maximum $C_{FL} = 0.10$

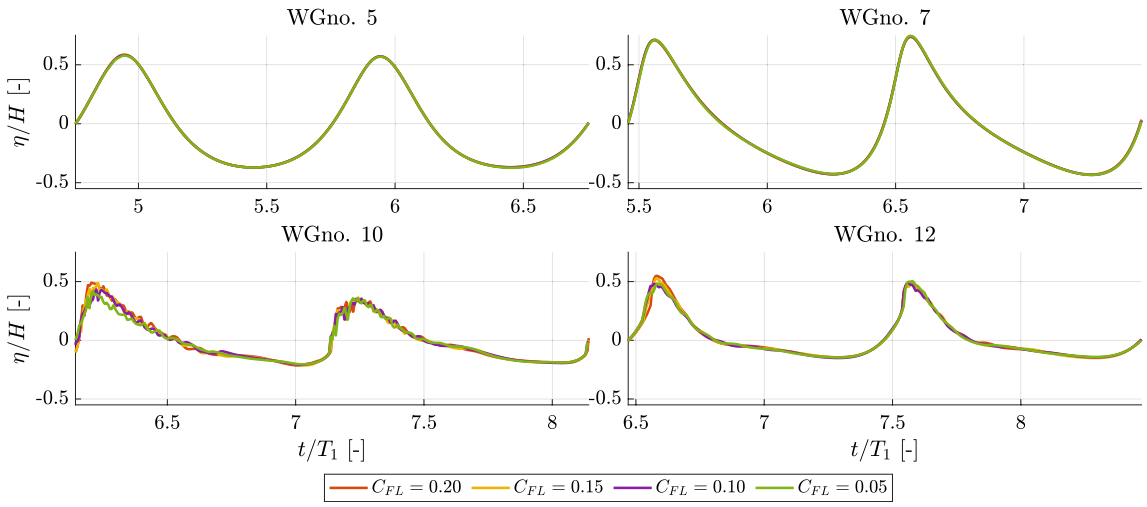

Fig. 43 Influence of the maximum C_{FL} on surface elevation time series for selected WGnos.; wave condition 3 and $N_{cH} = 30$

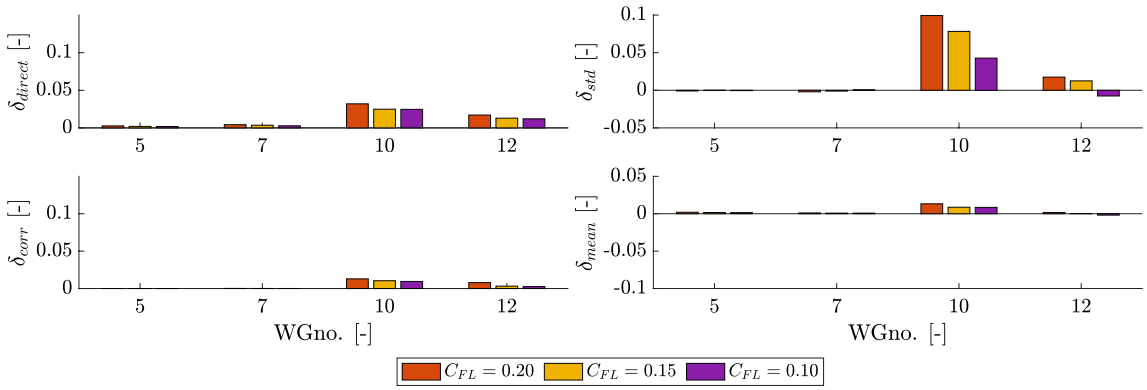

Fig. 44 Influence of the maximum C_{FL} on the evaluation metrics for selected WGnos.; wave condition 3 and $N_{cH} = 30$

A.2 Convergence of M-sigma (wave conditions 1–3)

The convergence with N_{cL} in wave conditions 1 and 2 can be seen in Figs. 45, 46 and Figs. 47, 48, respectively. With $N_{cL} = 60, N_{\sigma} \geq 5$ yielded negligible differences in both surface elevation time series and associated evaluation metrics ($< 1\%$) for wave conditions 1 and 2, and the variation herewith are therefore not included as figures. The convergence

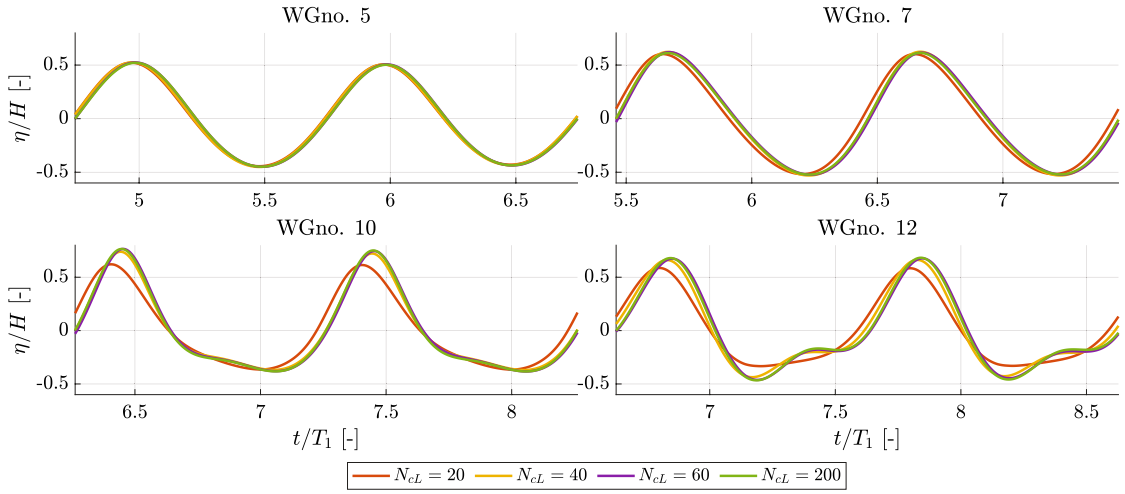

Fig. 45 Influence of N_{cL} on the surface elevation time series for selected WGnos.; wave condition 1 and $N_\sigma = 5$

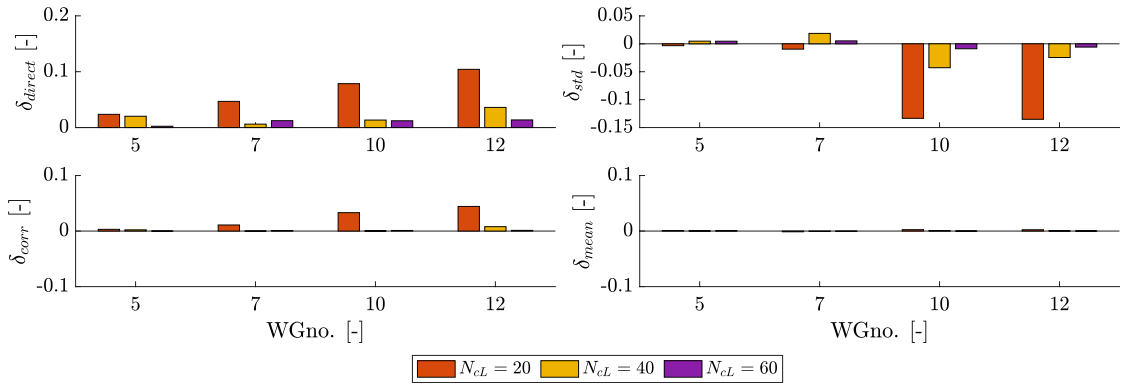

Fig. 46 Influence of N_{cL} on evaluation metrics for selected WGnos.; wave condition 1 and $N_\sigma = 5$

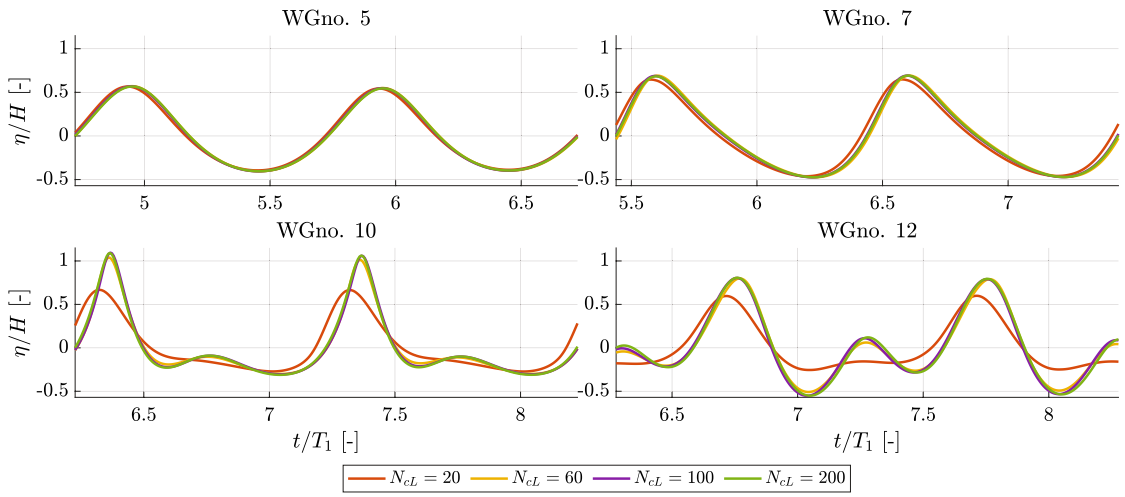

Fig. 47 Influence of N_{cL} on the surface elevation time series for selected WGnos.; wave condition 2 and $N_\sigma = 5$

with N_{cL} and N_σ in wave condition 3 can be seen in Figs. 49, 50, 51, 52. For wave condition 3, the crest height at $t/T_1 \approx 7.2$ recorded with WGno. 10 deviates with about 10% for $N_{cL} = 100$ relative to N_{cL}=200, whereas for $N_{cL} = 150$ the deviation is about 1%, see Fig. 49. Based on this $N_{cL} = 150$ is assessed sufficiently converged rather than $N_{cL} = 100$ despite of both having all evaluation metrics less than 5

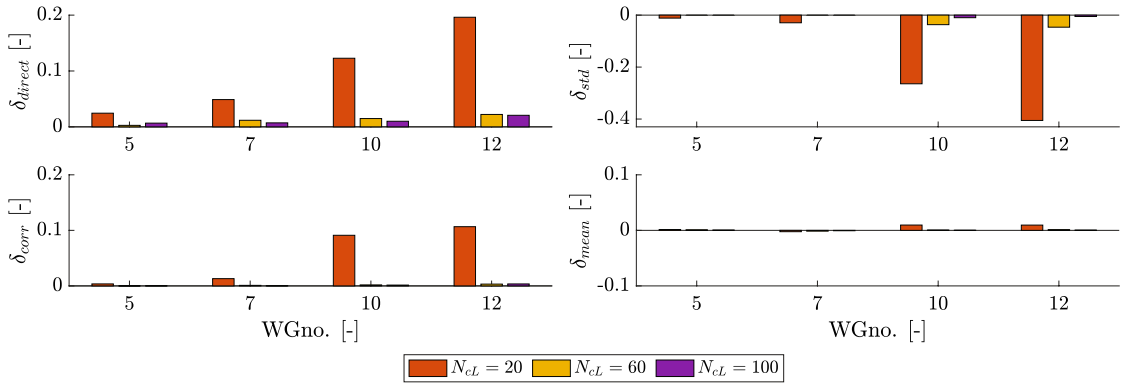

Fig. 48 Influence of N_{cL} on evaluation metrics for selected WGnos.; wave condition 2 and N_{σ} =5

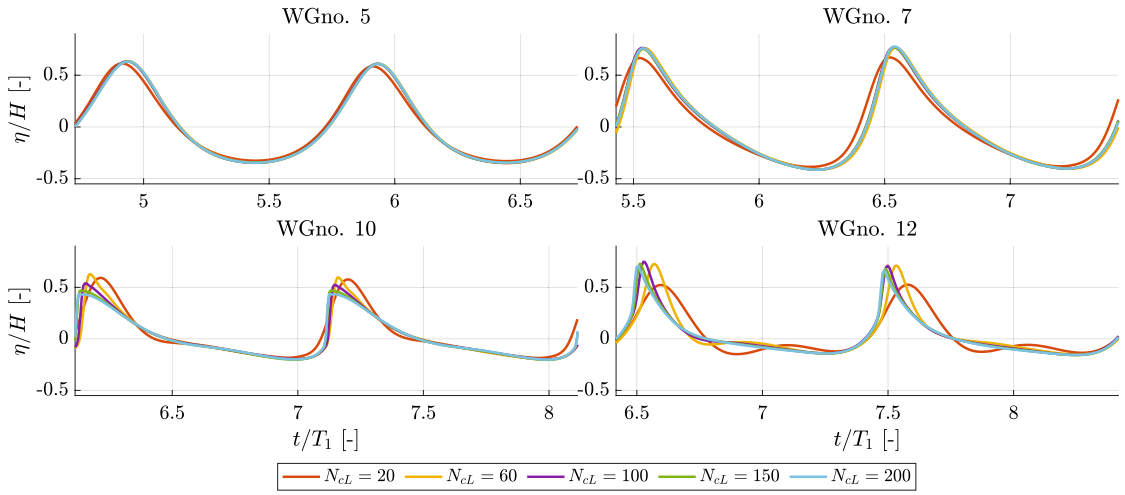

Fig. 49 Influence of N_{cL} on the surface elevation time series for selected WGnos.; wave condition 3 and $N_{\sigma} = 15$

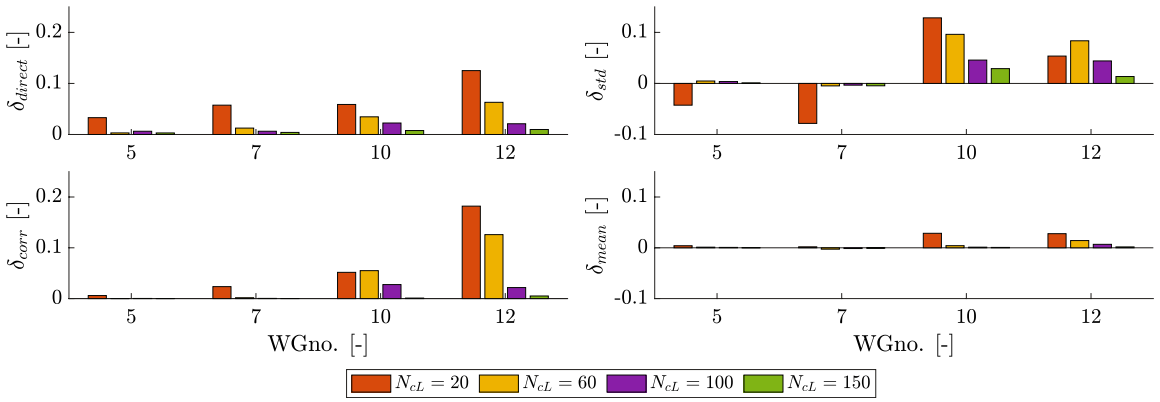

Fig. 50 Influence of N_{cL} on evaluation metrics for selected WGnos.; wave condition 3 and $N_{\sigma} = 15$

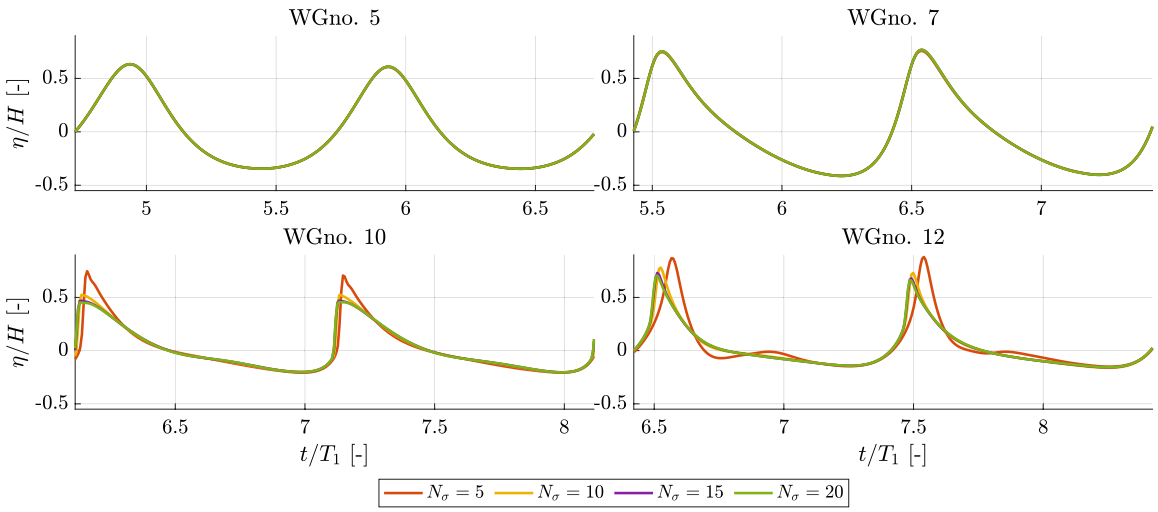

Fig. 51 Influence of N_σ on the surface elevation time series for selected WGnos.; wave condition 3 and $N_{cL} = 150$

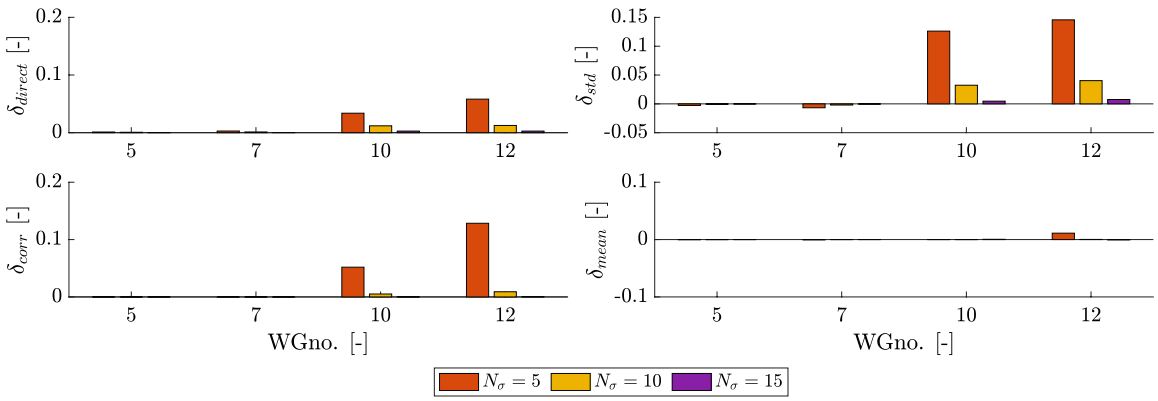

Fig. 52 Influence of N_σ on evaluation metrics for selected WGnos.; wave condition 3 and $N_{cL} = 150$

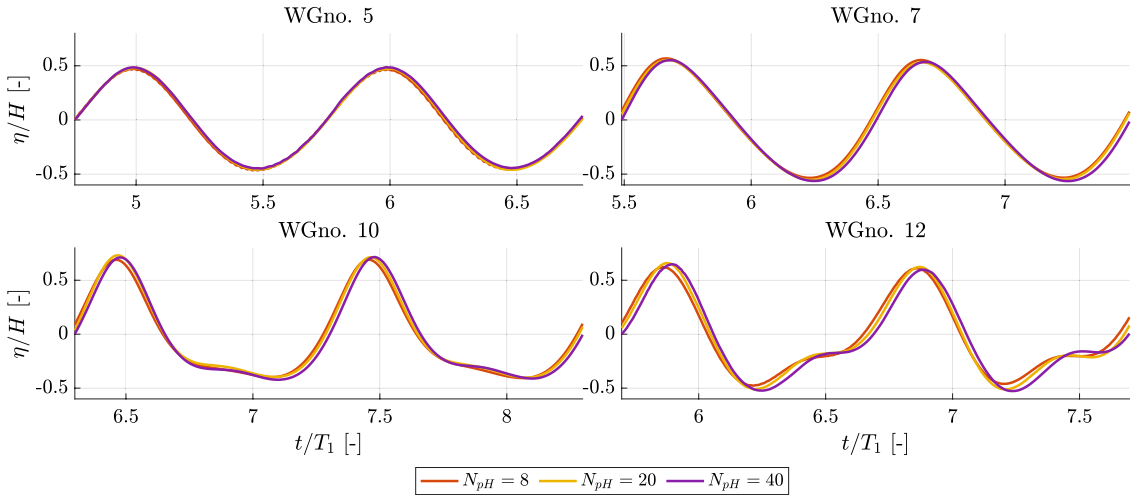

Fig. 53 Influence of N_{pH} on the surface elevation time series for selected WGnos.; wave condition 1

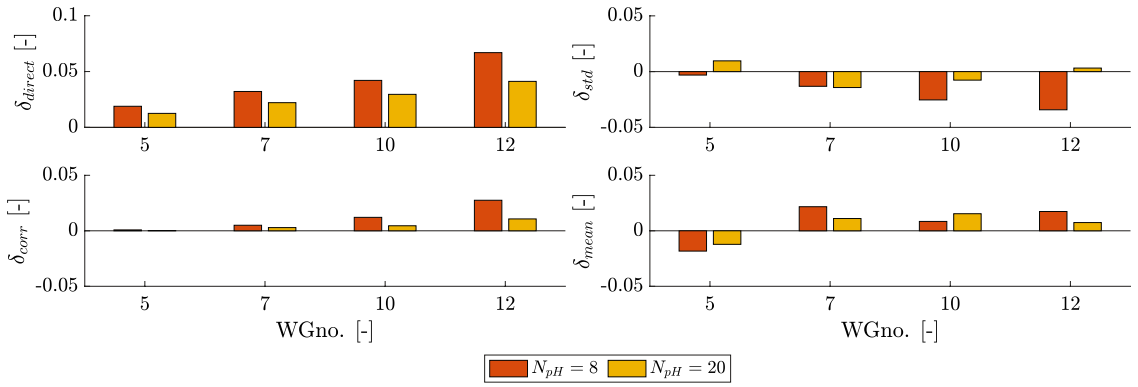

Fig. 54 Influence of N_{pH} on evaluation metrics for selected WGnos.; wave condition 1

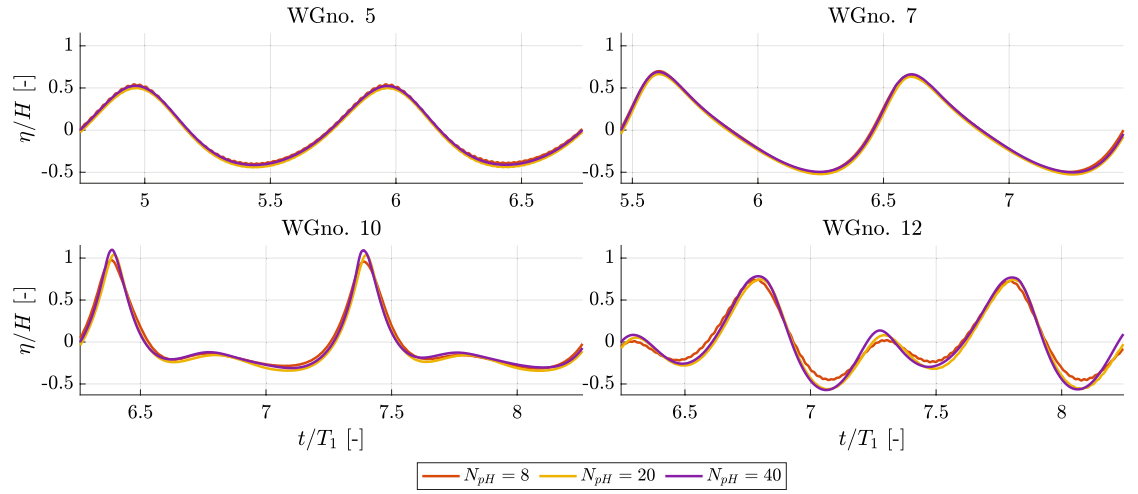

Fig. 55 Influence of N_{pH} on the surface elevation time series for selected WGnos.; wave condition 2

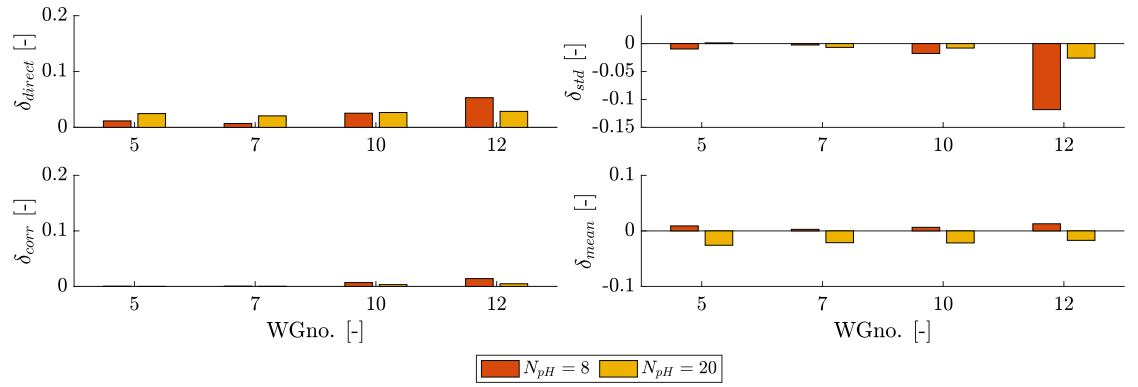

Fig. 56 Influence of N_{pH} on evaluation metrics for selected WGnos.; wave condition 2

A.3 Convergence of D-SPH (wave conditions 1–3)

The convergence of the D-SPH model with N_{cH} in wave conditions 1–3 can be seen in Figs. 53, 54, 55, 56, 57, 58. In wave conditions 1 and 2, $N_{pH} \geq 20$ yields only small differences in the surface elevation time series and all evaluation metrics are below 5%. Based on this D-SPH is assessed converged for $N_{pH} = 20$. Notable deviations and evaluations

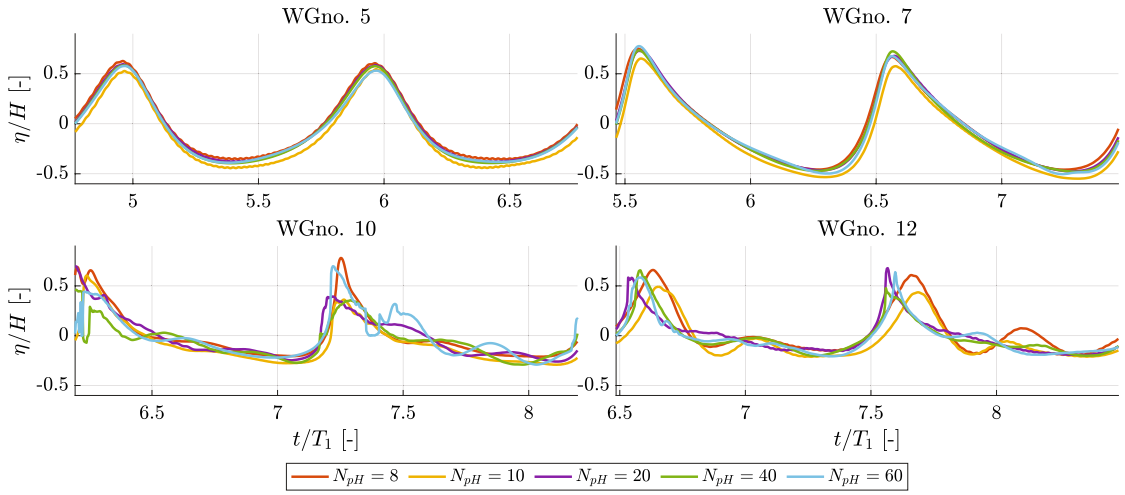

Fig. 57 Influence of N_{pH} on the surface elevation time series for selected WGnos.; wave condition 3

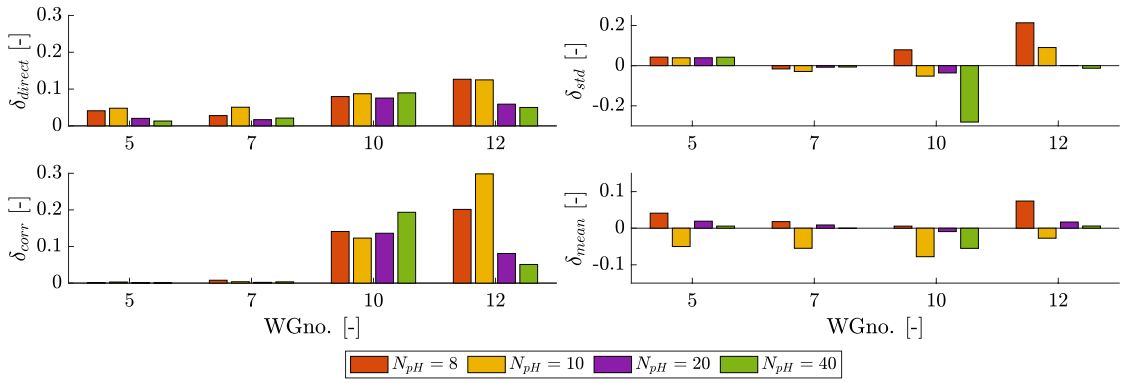

Fig. 58 Influence of N_{pH} on evaluation metrics for selected WGnos.; wave condition 3

metrics above 5% were present between $N_{pH} = 20$ and $N_{pH} = 40$ at WGnos. 10 and 12 in wave condition 3 from which an additional simulation with $N_{pH} = 60$ was completed. The surface elevation time series with $N_{pH} = 60$ was significantly more erratic at WGno. 10 than the simulations with $N_{pH} \in \{20, 40\}$. The convergence criteria imposed in the other convergence analyses (across numerical models) was thus not met for wave condition 3 as discussed in Sects. 6.3 and 8.3. Small variations in N_{pH} was found to have the potential to change results significantly in the breaking wave conditions which could have altered the conclusion of the convergence analysis of wave condition 3 but not removed the issue of inconsistency hereof.

Appendix B Density Field of the D-SPH model

As introduced in Sect. 6.3, the density field variations of the D-SPH model ought not exceed 1% relative to the nominal or initial density ρ_0 nor contain any significant discontinuities in order to represent a nearly incompressible fluid. In Figs. 59 and 60, the density field is shown over a wave period of the two breaking wave conditions 3 and 4, respectively. Here, it is demonstrated how the density field variations are limited to $\rho/\rho_0 < 1\%$ and, additionally, how the density field is continuous in space over the vast majority of the domain. Around the re-entry of the plunging jet some density field

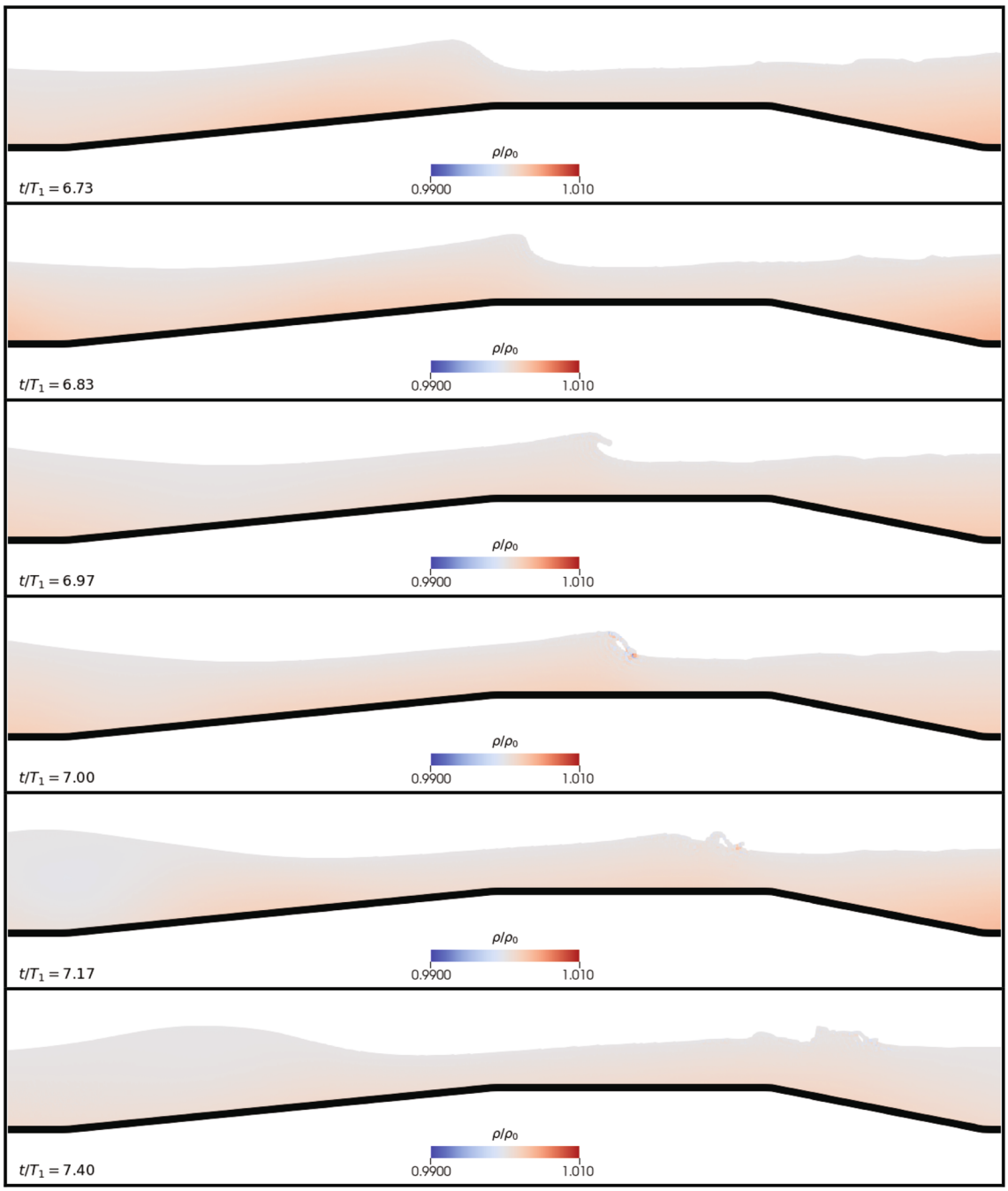

Fig. 59 Density field at selected time coordinates for wave breaking over the submerged bar in wave condition 3 with the D-SPH model

discontinuities exist as, e.g., can be seen from frames $t/T_1 \in \{7.00,\ 7.17\}$ in Fig. 59 and $t/T_1 \in \{7.13\}$ in Fig. 60. However, these discontinuities are highly local in time and space and thus limited to the region of the plunging jet impact. Outside this narrow region, spatial continuity is present. Mitigating said discontinuities to improve the representation of a nearly incompressible water phase could potentially increase the accuracy of the D-SPH model further. In future releases of DualSPHysics, this may be carried out by employing the two new schemes of Velocity-Divergence Error Mitigating (VEM) and the Volume Conservation Shifting (VCS) from Khayyer et al. [73]. This is outside the scope of the present paper.

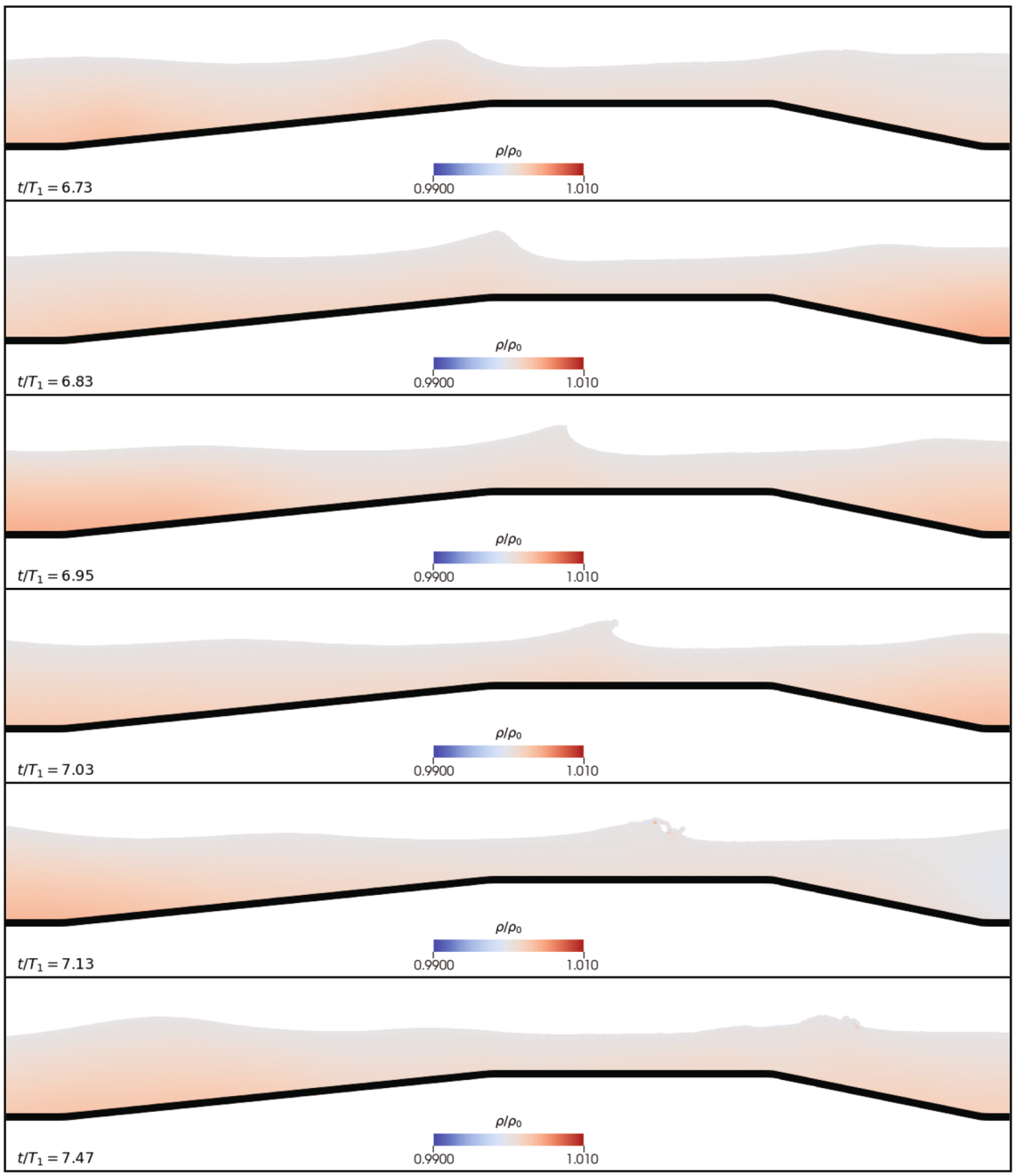

Fig. 60 Density field at selected time coordinates for wave breaking over the submerged bar in wave condition 4 with the D-SPH model

References

1. Klinge Jacobsen H, Hevia-Koch P, Wolter C. Nearshore and offshore wind development: costs and competitive advantage exemplified by nearshore wind in Denmark. Energy Sustain Dev. 2019;50:91–100. https://doi.org/10.1016/j.esd.2019.03.006.
2. Kantamaneni K, Rice L, Du X, Allali B, Yenneti K. Are current UK coastal defences good enough for tomorrow? An assessment of vulnerability to coastal erosion. Coast Manag. 2022;50(2):142–59. https://doi.org/10.1080/08920753.2022.2022971.
3. Dingemans MW. Comparison of computations with Boussinesq-like models and laboratory measurements. 1994.
4. Beji S, Battjes JA. Numerical simulation of nonlinear wave propagation over a bar. Coast Eng. 1994;23(1):1–16. https://doi.org/10.1016/0378-3839(94)90012-4.
5. Brocchini M, Drago M, Iovenitti L. The Modelling of Short Waves in Shallow Waters. Comparison of Numerical Models Based on Boussinesq and Serre Equations, pp. 76–88. https://doi.org/10.1061/9780872629332.006.
6. Kobayashi N, Otta AK, Roy I. Wave reflection and run-up on rough slopes. J Waterw Port Coast Ocean Eng. 1987;113(3):282–98. https://doi.org/10.1061/(ASCE)0733-950X(1987)113:3(282).
7. Roache PJ. Verification and validation in fluids engineering: some current issues. J Fluids Eng. 2016;138(10):101205. https://doi.org/10.1115/1.4033979.
8. Wroniszewski PA, Verschaeve J, Pedersen GK. Benchmarking of Navier-stokes codes for free surface simulations by means of a solitary wave. Coast Eng. 2014;91:1–17. https://doi.org/10.1016/j.coastaleng.2014.04.012.
9. Bhushan S, El Fajri O, Hubbard G, Chambers B, Kees C. Assessment of numerical methods for plunging breaking wave predictions. J Marine Sci Eng. 2021. https://doi.org/10.3390/jmse9030264.
10. Weller HG, Tabor G, Jasak H, Fureby C. A tensorial approach to computational continuum mechanics using object-oriented techniques. Comput Phys. 1998;12(6):620–31. https://doi.org/10.1063/1.168744 (https://pubs.aip.org/aip/cip/article-pdf/12/6/620/7865493/620_1_online.pdf).
11. Higuera P, Lara JL, Losada IJ. Simulating coastal engineering processes with OpenFOAM. Coast Eng. 2013;71:119–34. https://doi.org/10.1016/j.coastaleng.2012.06.002.
12. Stagonas D, Higuera P, Buldakov E. Simulating breaking focused waves in cfd: methodology for controlled generation of first and second order. J Waterw Port Coast Ocean Eng. 2018;144(2):06017005. https://doi.org/10.1061/(ASCE)WW.1943-5460.0000420.
13. Fernandez-Mora A, Ribberink JS, Zanden J, Werf JJ, Jacobsen NG. Rans-vof modeling of hydrodynamics and sand transport under full-scale non-breaking and breaking waves. Coast Eng Proc. 2017;1(35):29. https://doi.org/10.9753/icce.v35.sediment.29.
14. Torres-Freyermuth A, Losada IJ, Lara JL. Modeling of surf zone processes on a natural beach using Reynolds-averaged Navier-stokes equations. J Geophys Res Oceans. 2007. https://doi.org/10.1029/2006JC004050.
15. Li Y, Larsen BE, Fuhrman DR. Reynolds stress turbulence modelling of surf zone breaking waves. J Fluid Mech. 2022;937:7. https://doi.org/10.1017/jfm.2022.92.
16. Brown SA, Greaves DM, Magar V, Conley DC. Evaluation of turbulence closure models under spilling and plunging breakers in the surf zone. Coast Eng. 2016;114:177–93. https://doi.org/10.1016/j.coastaleng.2016.04.002.
17. Ting F, Kirby JT. Observation of undertow and turbulence in a laboratory surf zone. Coast Eng. 1994;24(1):51–80. https://doi.org/10.1016/0378-3839(94)90026-4.
18. Shih TH, Zhu J, Lumley JL. A realizable Reynolds stress algebraic equation model. 1993.
19. Schmitt P, Windt C, Davidson J, Ringwood JV, Whittaker T. Beyond vof: alternative openfoam solvers for numerical wave tanks. J Ocean Eng Marine Energy. 2020;6:277–92. https://doi.org/10.1007/s40722-020-00173-9.
20. Gruwez V, Altomare C, Suzuki T, Streicher M, Cappietti L, Kortenhaus A, Troch P. Validation of rans modelling for wave interactions with sea dikes on shallow foreshores using a large-scale experimental dataset. J Marine Sci Eng. 2020. https://doi.org/10.3390/jmse8090650.
21. Larsen BE, Fuhrman DR, Roenby J. Performance of interFoam on the simulation of progressive waves. Coast Eng J. 2019;61(3):380–400. https://doi.org/10.1080/21664250.2019.1609713.
22. Pedersen J, Larsen B, Bredmose H, Jasak H. A new Volume-of-Fluid method in OpenFOAM. In: Visonneau M, Queutey P., Le Touzé D (eds) MARINE 2017 computational methods in marine engineering VII, pp. 266–278. International Center for Numerical Methods in Engineering, 2017. 7th International conference on computational methods in marine engineering, MARINE 2017, 15–17 May 2017.
23. Vukčević V, Jasak H, Gatin I. Implementation of the ghost fluid method for free surface flows in polyhedral finite volume framework. Comput Fluids. 2017;153:1–19. https://doi.org/10.1016/j.compfluid.2017.05.003.
24. Qwist J, Christensen ED. Development and implementation of a direct surface description method for free surface flows in OpenFOAM. Coast Eng. 2023;179:104227. https://doi.org/10.1016/j.coastaleng.2022.104227.
25. Ma G, Shi F, Kirby JT. Shock-capturing non-hydrostatic model for fully dispersive surface wave processes. Ocean Model. 2012;43–44:22–35. https://doi.org/10.1016/j.ocemod.2011.12.002.
26. Lin P, Li CW. A σ-coordinate three-dimensional numerical model for surface wave propagation. Int J Numer Meth Fluids. 2002;38(11):1045–68. https://doi.org/10.1002/fld.258.
27. DHI: MIKE 3 Wave Model FM. https://www.mikepoweredbydhi.com/products/mike-3-wave-fm.
28. Hicks JBH. Development of a high-order potential flow solver for nonlinear wave-structure interaction. PhD thesis, Technical University of Denmark.
29. Domínguez JM, Fourtakas G, Altomare C, Canelas RB, Tafuni A, García-Feal O, Martínez-Estévez I, Mokos A, Vacondio R, Crespo A, Rogers BD, Stansby PK, Gómez-Gesteira M. DualSPHysics: from fluid dynamics to multiphysics problems. Comput Particle Mech. 2022;9:867–95. https://doi.org/10.1007/s40571-021-00404-2.
30. Lowe RJ, Buckley ML, Altomare C, Rijnsdorp DP, Yao Y, Suzuki T, Bricker JD. Numerical simulations of surf zone wave dynamics using smoothed particle hydrodynamics. Ocean Model. 2019;144:101481. https://doi.org/10.1016/j.ocemod.2019.101481.
31. Zhang F, Crespo A, Altomare C, Domínguez J, Marzeddu A, Shang S-P, Gómez-Gesteira M. DualSPHysics: a numerical tool to simulate real breakwaters. J Hydrodyn. 2018;30:95–105. https://doi.org/10.1007/s42241-018-0010-0.

32. Domínguez JM, Crespo A, Hall M, Altomare C, Wu M, Stratigaki V, Troch P, Cappietti L, Gómez-Gesteira M. SPH simulation of floating structures with moorings. Coast Eng. 2019;153:103560. https://doi.org/10.1016/j.coastaleng.2019.103560.
33. Antuono M, Colagrossi A, Marrone S. Numerical diffusive terms in weakly-compressible SPH schemes. Comput Phys Commun. 2012;183:2570–80. https://doi.org/10.1016/j.cpc.2012.07.006.
34. Vacondio R, Altomare C, Leffe MD, Hu X, Touzé DL, Lind S, Marongiu J-C, Marrone S, Rogers BD, Souto-Iglesias A. Grand challenges for smoothed particle hydrodynamics numerical schemes. Comput Particle Mech. 2021;8:575–88. https://doi.org/10.1007/s40571-020-00354-1.
35. González-Cao J, Altomare C, Crespo A, Domínguez JM, Gómez-Gesteira M, Kisacik D. On the accuracy of DualSPHysics to assess violent collisions with coastal structures. Comput Fluids. 2019;179:604–12. https://doi.org/10.1016/j.compfluid.2018.11.021.
36. Park H, Do T, Tomiczek T, Cox DT, Lindt JW. Numerical modeling of non-breaking, impulsive breaking, and broken wave interaction with elevated coastal structures: Laboratory validation and inter-model comparisons. Ocean Eng. 2018;158:78–98. https://doi.org/10.1016/j.oceaneng.2018.03.088.
37. Kamath A, Bihs H, Chella MA. A Arntsen: CFD simulations of wave propagation and shoaling over a submerged bar. Aquatic Procedia. 2015;4:308–16. https://doi.org/10.1016/j.aqpro.2015.02.042.
38. Gadelho J, Lavrov A, Soares CG. Modelling the Effect of Obstacles on the 2D Wave Propagation with OpenFOAM.
39. Andersen J, Eldrup MR, Ferri F, Verao Fernandez G. Wave propagation over a submerged bar: datasets from wave flume experiments and CFD. Zenodo (2025). https://doi.org/10.5281/zenodo.15049542.
40. Zhang H, Schäffer HA. Approximate stream function wavemaker theory for highly non-linear waves in wave flumes. Ocean Eng. 2007;34:1290–302. https://doi.org/10.1016/J.OCEANENG.2006.04.010.
41. Schäffer HA. Second-order wavemaker theory for irregular waves. Ocean Eng. 1996;23(1):47–88. https://doi.org/10.1016/0029-8018(95)00013-B.
42. Eldrup MR, Andersen TL. Applicability of nonlinear wavemaker theory. J Marine Sci Eng. 2019. https://doi.org/10.3390/jmse7010014.
43. OpenCFD Ltd: OpenCFD. https://www.openfoam.com/.
44. Brown SA, Magar V, Greaves DM, Conley DC. An evaluation of RANS turbulence closure models for spiling breakers. Coast Eng Proc. 2014;1:5. https://doi.org/10.9753/icce.v34.waves.5.
45. Deshpande SS, Anumolu L, Trujillo MF. Evaluating the performance of the two-phase flow solver interFoam. Comput Sci Discov. 2012. https://doi.org/10.1088/1749-4699/5/1/014016.
46. Jacobsen NG, Fuhrman DR, Fredsøe J. A wave generation toolbox for the open-source CFD library: OpenFOAM®. Int J Numer Meth Fluids. 2012;70:1073–88. https://doi.org/10.1002/fld.2726.
47. Fuhrman D, Madsen P, Bingham HB. Numerical simulation of lowest-order short-crested wave instabilities. J Fluid Mech. 2006;563:415–41. https://doi.org/10.1017/S0022112006001236.
48. Fenton JD. The numerical solution of steady water wave problems. Comput Geosci. 1988;14:357–68. https://doi.org/10.1016/0098-3004(88)90066-0.
49. Madsen P, Fuhrman D. Third-order theory for bichromatic bi-directional water waves. J Fluid Mech. 2006;557:369–97. https://doi.org/10.1017/S0022112006009815.
50. Lin P, Liu PL-F. A numerical study of breaking waves in the surf zone. J Fluid Mech. 1998;359:239–64. https://doi.org/10.1017/S002211209700846X.
51. Larsen J, Dancy H. Open boundaries in short wave simulations—a new approach. Coast Eng. 1983;7:285–97.
52. DHI: MIKE 3 Wave Model FM. Hydrodynamic Module and Sand Transport User Guide.
53. DHI: MIKE 3 Wave Model FM. Hydrodynamic Module. Scientific Documentaiton.
54. Toro EF, Spruce M, Speares W. Restoration of the contact surface in the HLL-Riemann solver. Shock Waves. 1994;4:25–34. https://doi.org/10.1007/BF01414629.
55. Rodi W. Turbulence models and their application in hydraulics—a state of the art review. IAHR, 1980.
56. Rodi W. Turbulence models and their application in hydraulics. IAHR, 1984.
57. Larsen BE, Fuhrman DR. On the over-production of turbulence beneath surface waves in Reynolds-averaged Navier-stokes models. J Fluid Mech. 2018;853:419–60. https://doi.org/10.1017/jfm.2018.577.
58. Wendland H. Piecewise polynomial, positive definite and compactly supported radial functions of minimal degree. Adv Comput Math. 1995;4:389–96. https://doi.org/10.1007/BF02123482.
59. Fourtakas G, Dominguez JM, Vacondio R, Rogers BD. Local uniform stencil (LUST) boundary condition for arbitrary 3-D boundaries in parallel smoothed particle hydrodynamics (SPH) models. Comput Fluids. 2019;190:346–61. https://doi.org/10.1016/j.compfluid.2019.06.009.
60. Monaghan JJ. Smoothed particle hydrodynamics. Ann Rev Astron Astrophys. 1992;30:543–74. https://doi.org/10.1146/annurev.aa.30.090192.002551.
61. Monaghan JJ. Simulating free surface flows with SPH. J Comput Phys. 1994;110:399–406. https://doi.org/10.1006/jcph.1994.1034.
62. Hughes SA. Physical models and laboratory techniques in coastal engineering. World Sci. 1993. https://doi.org/10.1142/2154.
63. Altomare C, Domínguez JM, Crespo A, González-Cao J, Suzuki T, Gómez-Gesteira M, Troch P. Long-crested wave generation and absorption for SPH-based DualSPHysics model. Coast Eng. 2017;127:37–54. https://doi.org/10.1016/j.coastaleng.2017.06.004.
64. English A, Domínguez JM, Vacondio R, Crespo AJC, Stansby PK, Lind SJ, Chiapponi L, Gómez-Gesteira M. Modified dynamic boundary conditions (mDBC) for general-purpose smoothed particle hydrodynamics (SPH): application to tank sloshing, dam break and fish pass problems. Comput Particle Mech. 2021. https://doi.org/10.1007/s40571-021-00403-3.
65. BIMP, IEC, IFCC, ILAC, ISO, IUPAC, IUPAP, OIML: 100:2008 Evaluation of Measurement Data-Guide to the Expression of Uncertainty in Measurement. https://www.bipm.org/documents/20126/2071204/JCGM_100_2008_E.pdf/cb0ef43f-baa5-11cf-3f85-4dcd86f77bd6.
66. Krystek M, Anton M. A weighted total least-squares algorithm for fitting a straight line. Meas Sci Technol. 2007;18:3438. https://doi.org/10.1088/0957-0233/18/11/025.

67. Kramer MB, Andersen J, Thomas S, Bendixen FB, Bingham H, Read R, Holk N, Ransley E, Brown S, Yu Y-H, Tran TT, Davidson J, Horvath C, Janson C-E, Nielsen K, Eskilsson C. Highly accurate experimental heave decay tests with a floating sphere: A public benchmark dataset for model validation of fluid-structure interaction. Energies. 2021. https://doi.org/10.3390/en14020269.
68. Altomare C, Crespo A, Domínguez JM, Gómez-Gesteira M, Suzuki T, Verwaest T. Applicability of smoothed particle hydrodynamics for estimation of sea wave impact on coastal structures. Coast Eng. 2015;96:1–12. https://doi.org/10.1016/j.coastaleng.2014.11.001.
69. Gruwez V, Altomare C, Suzuki T, Streicher M, Cappietti L, Kortenhaus A, Troch P. An inter-model comparison for wave interactions with sea dikes on shallow foreshores. J Marine Sci Eng. 2020. https://doi.org/10.3390/jmse8120985.
70. Padova DD, Dalrymple RA, Mossa M. Analysis of the artificial viscosity in the smoothed particle hydrodynamics modelling of regular waves. J Hydraul Res. 2014;52:836–48. https://doi.org/10.1080/00221686.2014.932853.
71. Roselli R, Vernengo G, Altomare C, Brizzolara S, Bonfiglio L, Guercio R. Ensuring numerical stability of wave propagation by tuning model parameters using genetic algorithms and response surface methods. Environ Model Softw. 2018;103:62–73. https://doi.org/10.1016/j.envsoft.2018.02.003.
72. Lowe RJ, Buckley ML, Altomare C, Rijnsdorp DP, Yao Y, Suzuki T, Bricker JD. Numerical simulations of surf zone wave dynamics using smoothed particle hydrodynamics. Ocean Model. 2019;144:101481. https://doi.org/10.1016/j.ocemod.2019.101481.
73. Khayyer A, Shimizu Y, Gotoh T, Gotoh H. Enhanced resolution of the continuity equation in explicit weakly compressible SPH simulations of incompressible free-surface fluid flows. Appl Math Model. 2023;116:84–121. https://doi.org/10.1016/j.apm.2022.10.037.
74. Altomare C, Scandura P, Cáceres IA, D.A., Viccione G. Large-scale wave breaking over a barred beach: SPH numerical simulation and comparison with experiments. Coast Eng. 2023;185:104362. https://doi.org/10.1016/j.coastaleng.2023.104362.
75. Pellegrini F, Roman J. Scotch: a software package for static mapping by dual recursive bipartitioning of process and architecture graphs, 1996; 493–498.
76. Axtmann G, Rist U. Scalability of OpenFOAM with large eddy simulations and DNS on high-performance systems. High Performance Comput Sci Eng. 2016;16:413–24. https://doi.org/10.13140/RG.2.1.2395.8000.
77. Karypis G, Kumar V. A fast and high quality multilevel scheme for partitioning irregular graphs. SIAM J Sci Comput. 1998;20:359–92. https://doi.org/10.1137/S1064827595287997.
78. Eldrup MR, Andersen TL. Numerical study on regular wave shoaling, de-shoaling and decomposition of free/bound waves on gentle and steep foreshores. J Marine Sci Eng. 2020. https://doi.org/10.3390/jmse8050334.
79. Holthuijsen LH. Waves in oceanic and coastal waters. Cambridge University Press, 2007. https://doi.org/10.1017/CBO9780511618536.
80. Beji S, Battjes JA. Experimental investigation of wave propagation over a bar. Coast Eng. 1993;19:151–62. https://doi.org/10.1016/0378-3839(93)90022-Z.
81. Quinlan NJ, Basa M, Lastiwka M. Truncation error in mesh-free particle methods. Int J Numer Meth Eng. 2006;66:2064–85. https://doi.org/10.1002/nme.1617.
82. Vacondio R, Rogers BD, Stansby PK, Mignosa P, Feldman J. Variable resolution for SPH: a dynamic particle coalescing and splitting scheme. Comput Methods Appl Mech Eng. 2013;256:132–48. https://doi.org/10.1016/j.cma.2012.12.014.
83. Khayyer A, Gotoh H, Shimizu Y. A projection-based particle method with optimized particle shifting for multiphase flows with large density ratios and discontinuous density fields. Comput Fluids. 2019;179:356–71. https://doi.org/10.1016/j.compfluid.2018.10.018.